

Are local ULIRGs powered by AGN? The sub-kpc view of the 220 GHz continuum. PUMA II

M. Pereira-Santaella¹, L. Colina¹, S. García-Burillo², I. Lamperti¹, E. González-Alfonso³, M. Perna^{1,4}, S. Arribas¹, A. Alonso-Herrero⁵, S. Aalto⁶, F. Combes⁷, A. Labiano⁵, J. Piqueras-López¹, D. Rigopoulou⁸, and P. van der Werf⁹

¹ Centro de Astrobiología (CSIC-INTA), Ctra. de Ajalvir, Km 4, 28850, Torrejón de Ardoz, Madrid, Spain
e-mail: miguel.pereira@cab.inta-csic.es

² Observatorio Astronómico Nacional (OAN-IGN)-Observatorio de Madrid, Alfonso XII, 3, 28014, Madrid, Spain

³ Universidad de Alcalá, Departamento de Física y Matemáticas, Campus Universitario, 28871 Alcalá de Henares, Madrid, Spain

⁴ INAF - Osservatorio Astrofisico di Arcetri, Largo Enrico Fermi 5, I-50125 Firenze, Italy

⁵ Centro de Astrobiología (CSIC-INTA), ESAC Campus, E-28692 Villanueva de la Cañada, Madrid, Spain

⁶ Department of Space, Earth and Environment, Onsala Space Observatory, Chalmers University of Technology, 439 92 Onsala, Sweden

⁷ LERMA, Obs. de Paris, PSL Univ., Collège de France, CNRS, Sorbonne Univ., Paris, France

⁸ Department of Physics, University of Oxford, Keble Road, Oxford OX1 3RH, UK

⁹ Leiden Observatory, Leiden University, PO Box 9513, 2300, RA Leiden, The Netherlands

May 11, 2021

ABSTRACT

We analyze new high-resolution (400 pc) ~ 220 GHz continuum and CO(2–1) ALMA observations of a representative sample of 23 local ($z < 0.165$) ULIRG systems (34 individual nuclei) as part of the “Physics of ULIRGs with MUSE and ALMA” (PUMA) project. The deconvolved half-light radii of the ~ 220 GHz continuum sources, r_{cont} , are between < 60 pc and 350 pc (median 80–100 pc). We associate these regions with the regions emitting the bulk of the infrared luminosity (L_{IR}). The good agreement, within a factor of 2, between the observed ~ 220 GHz fluxes and the extrapolation of the infrared gray-body, and the small contributions from synchrotron and free-free emission support this assumption. The cold molecular gas emission sizes, r_{CO} , are between 60 and 700 pc and are similar in advanced mergers and early interacting systems. On average, r_{CO} are ~ 2.5 times larger than r_{cont} . Using these measurements, we derive the nuclear L_{IR} and cold molecular gas surface densities ($\Sigma_{L_{\text{IR}}} = 10^{11.5} - 10^{14.3} L_{\odot} \text{ kpc}^{-2}$ and $\Sigma_{\text{H}_2} = 10^{2.9} - 10^{4.2} M_{\odot} \text{ pc}^{-2}$, respectively). Assuming that the L_{IR} is produced by star-formation, the median $\Sigma_{L_{\text{IR}}}$ corresponds to $\Sigma_{\text{SFR}} = 2500 M_{\odot} \text{ yr}^{-1} \text{ kpc}^{-2}$. This Σ_{SFR} implies extremely short depletion times, $\Sigma_{\text{H}_2}/\Sigma_{\text{SFR}} < 1\text{--}15$ Myr, and unphysical star-formation efficiencies > 1 for 70% of the sample. Therefore, this favors the presence of an obscured AGN in these objects that could dominate the L_{IR} . We also classify the ULIRG nuclei in two groups: (a) compact nuclei ($r_{\text{cont}} < 120$ pc) with high mid-IR excess emission ($\Delta L_{6-20\mu\text{m}}/L_{\text{IR}}$) found in optically classified AGN; and (b) nuclei following a relation with decreasing $\Delta L_{6-20\mu\text{m}}/L_{\text{IR}}$ for decreasing r_{cont} . The majority, 60%, of the nuclei in interacting systems lie in the low- r_{cont} end (< 120 pc) of this relation, while only 30% of the mergers do so. This suggests that in the early stages of the interaction, the activity occurs in a very compact and dust-obscured region while, in more advanced merger stages, the activity is more extended, unless an optically detected AGN is present. Approximately two thirds of the nuclei have nuclear radiation pressures above the Eddington limit. This is consistent with the ubiquitous detection of massive outflows in local ULIRGs and supports the importance of the radiation pressure in the outflow launching process.

Key words. Galaxies: evolution – Galaxies: interactions – Galaxies: nuclei – Infrared: galaxies

1. Introduction

Ultraluminous infrared galaxies (ULIRGs; $L_{\text{IR}} > 10^{12} L_{\odot}$) are among the most luminous objects in the local Universe. The majority of local ULIRGs are major gas-rich mergers at different evolutionary stages: from interacting systems with two nuclei separated by few kpc to more advanced mergers with a single nucleus (see Lonsdale et al. 2006 and references therein). A classic evolutionary scenario suggests that merging ULIRGs evolve into a quasar that quenches the star-formation (SF) and, after that, the merger remnant becomes an intermediate-mass elliptical galaxy (e.g., Sanders et al. 1988; Springel et al. 2005). However, recent observations and simulations indicate that mergers do not always quench the SF and also that disks can regrow in mergers remnants (e.g., Ueda et al. 2014; Weigel et al. 2017; Weinberger et al. 2018). This suggests that ULIRGs can have

more varied evolutionary paths than that suggested by the classic scenario. Local ULIRGs might also be scaled down versions of the dusty star-forming mergers detected at $z > 2$ (e.g., Casey et al. 2014). Therefore, local ULIRGs are excellent targets for detailed studies of the physical processes that shape the, possibly diverse, evolutionary paths of merging gas-rich galaxies, which were important in the high- z universe.

One key property of local ULIRGs are their extremely compact (< 1 kpc; e.g., Condon et al. 1991; Soifer et al. 2000) and dust obscured nuclei ($A_V > 1000$ mag in some cases based on their nuclear molecular gas column densities; e.g., González-Alfonso et al. 2015). Because of this extreme obscuration most of the radiation produced in their nuclei, either by an active galactic nucleus (AGN) or by SF, is absorbed by dust and re-emitted in the infrared (IR) spectral range. For this reason, it is not straightforward to determine the dominant power source

(AGN vs. SF) of local ULIRGs. Mid-IR studies, which are less affected by extinction than optical and near-IR works, suggest that ULIRGs are mostly powered by SF (e.g., [Genzel et al. 1998](#)), although the AGN contribution increases with increasing luminosities (e.g., [Nardini et al. 2008](#); [Veilleux et al. 2009](#)). However, for $A_V > 1000$ mag, the mid-IR extinction is still very high, $A_{15\mu\text{m}} > 50$ mag (e.g., [Jiang et al. 2006](#)), and a large part of the emission could be completely obscured even in the mid-IR which. This could prevent an accurate determination of the AGN and SF contributions to the L_{IR} of local ULIRGs using mid-IR observations.

Alternatively, it is possible to investigate what powers local ULIRGs by measuring the size of the region that emits the bulk of the L_{IR} as well as the molecular gas content (i.e., the fuel for SF) of this region. These quantities are needed to determine the nuclear IR luminosity and gas surface densities. Finding IR luminosity densities well above the limit of a maximal starburst (e.g., [Thompson et al. 2005](#)) can be used to infer the presence of an obscured AGN and to estimate its luminosity (see e.g., [Downes & Eckart 2007](#); [Imanishi et al. 2011](#); [Sakamoto et al. 2017](#)).

In this paper, we analyze high-resolution (~ 400 pc) ALMA CO(2–1) and ~ 220 GHz continuum observations of sample of 23 local ULIRGs. We measure the size of the ~ 220 GHz ($\sim 1400 \mu\text{m}$) continuum, which we link with the bulk of the L_{IR} in these sources, and we estimate the nuclear cold molecular gas content from the CO(2–1) emission. We use these results to calculate their nuclear luminosity and molecular gas densities.

These ALMA observations of a representative sample of local ULIRGs are part of the “Physics of ULIRGs with MUSE and ALMA” (PUMA) project. The main goals of this project are: a) to establish the impact of massive outflows in the evolution of ULIRGs (negative and positive feedback); and b) to determine what drives this feedback (AGN vs. SF) during the entire merging process (from early stages to advanced mergers). To do so, we combine sub-kpc resolution adaptive optics-assisted VLT/MUSE optical integral field spectroscopy and CO(2–1) ALMA data to trace the multi-phase structure of the massive outflows as well as to investigate basic properties of the ULIRGs like their main power source. The first MUSE results on the spatially resolved stellar kinematics and the ionized outflow phase were presented by [Perna et al. \(2021\)](#) while the detailed analysis of the Arp 220 MUSE data was presented in [Perna et al. \(2020\)](#). Likewise, [Pereira-Santaella et al. \(2018\)](#) presented the first ALMA results on the spatially resolved cold molecular outflows detected in three of these local ULIRGs.

The paper is organized as follows. We briefly describe the PUMA sample in Sect. 2. The ALMA observations and data reduction are presented in Sect. 3. In Sect. 4, we derive the spatial properties of the ~ 220 GHz continuum and the CO(2–1) emission, and fit the IR and radio spectral energy distributions (SEDs) of the ULIRGs. Sect. 5 investigates the origin of the high luminosity and molecular gas surface densities in the ULIRG nuclei, the relation between the ~ 220 GHz continuum size with the mid-IR excess emission, the $9.7 \mu\text{m}$ silicate absorption, and the broad-band IRAS colors. We also estimate the radiation pressure in these nuclei. The main conclusions are summarized in Sect. 6.

Throughout this article we assume the following cosmology: $H_0 = 70 \text{ km s}^{-1} \text{ Mpc}^{-1}$, $\Omega_m = 0.3$, and $\Omega_\Lambda = 0.7$.

2. Sample of local ULIRGs

The PUMA sample is a volume-limited ($z < 0.165$; $d < 800$ Mpc) representative sample of 25 local ULIRGs (38 individual nuclei).

These objects were selected to examine the most relevant parameters for the feedback processes: (1) the main power source (AGN vs. SF); (2) the interaction stage (from interacting pairs to advanced mergers); and (3) the IR luminosity. The parent sample is the 1 Jy ULIRG sample ([Kim et al. 1998](#)) extended to southern objects by [Duc et al. \(1997\)](#). Our sample is limited to objects with Dec. between -65° and $+25^\circ$ which is appropriate for ALMA. We selected 12 interacting systems (nuclear separation > 1 kpc) and 13 mergers with nuclear separations < 1 kpc. Half of the objects in each interaction stage category were selected to be dominated by AGN based on mid-IR spectroscopy ([Veilleux et al. 2009](#); [Spoon et al. 2013](#)). The selected objects uniformly cover the ULIRG luminosity range between $10^{12.0}$ and $10^{12.7} L_\odot$. See Table 1 and [Perna et al. \(2021\)](#) for more details.

So far, we have obtained ALMA CO(2–1) and ~ 220 GHz continuum observations for 92% of the systems in the sample (23 systems with 34 individual nuclei). The CO(2–1) emission is detected in 33 nuclei and the continuum in 29 (see Sect. 4). In addition to our VLT/MUSE-AO optical integral field spectroscopy ([Perna et al. 2020, 2021](#)), the majority of the targets have extensive ancillary multi-wavelength data which include mid- and far-IR (e.g., [Veilleux et al. 2009](#); [Spoon et al. 2013](#); [Pearson et al. 2016](#); [Chu et al. 2017](#)), radio (e.g., [Condon et al. 1998](#); [Helfand et al. 2015](#)), and X-ray (e.g., [Iwasawa et al. 2011](#); [Teng et al. 2015](#)) observations.

3. Observations and data reduction

3.1. ALMA observations

We obtained ALMA 12-m array CO(2–1) 230.538 GHz and continuum observations for 23 out of the 25 PUMA ULIRGs. ALMA observations for the remaining two ULIRGs have been scheduled but are not available at the time of writing. These observations were mainly conducted as part of our programs 2015.1.00263.S, 2016.1.00170.S, and 2018.1.00699.S (PI: M. Pereira-Santaella). For 13120–5453 and F15327+2340 (Arp 220), we used archive data from programs 2016.1.00777.S (PI: K. Sliwa) and 2015.1.00113.S (PI: N. Scoville), respectively. In addition, we complemented this dataset with higher angular resolution data for 17208–0014 from program 2018.1.00486.S (PI: M. Pereira-Santaella). Observations of three of the ULIRGs in our sample (F12112+0305, F14348–1447, and F22491–1808) have been already presented in [Pereira-Santaella et al. \(2018\)](#), but we include them here for completeness.

We aimed to have a similar spatial resolution of ~ 400 pc in all the systems, so the synthesized beam full-width half-maximum (FWHM) varies between $0''.12$ and $1''$ depending on the distance of each target. We used a single 12-m array configuration with baselines set to achieve the required angular resolution. The maximum recoverable scale is about 10 times the beam FWHM (i.e., 4 kpc). Depending on the redshift, the CO(2–1) transition lies in the ALMA Band 5 or Band 6. Details on the observations are listed in Table 2.

We defined four 1.875 GHz bandwidth spectral windows with 2 to 8 MHz ($3\text{--}10 \text{ km s}^{-1}$) channels, depending on the targeted spectral feature. One spectral window was centered at the sky frequency of $^{12}\text{CO}(2\text{--}1)$ 230.538 GHz. The remaining spectral windows were centered at the frequency of nearby transitions (e.g., CS(5–4), H₃O α , SiO(5–4)) when possible or at a “line-free” spectral range.

We used the ALMA reduction software CASA (v5.6.1; [McMullin et al. 2007](#)) to calibrate the data using the standard

Table 1: Sample of local ULIRGs

IRAS name	Nucleus	R.A. ^a (ICRS)	Dec. ^a (ICRS)	v_{CO}^b (km s ⁻¹)	z^c	d_L^d (Mpc)	Scale ^d (kpc arcsec ⁻¹)	$\log L_{\text{IR}}^e$ (L_\odot)	Class. ^f	Morph. ^g
00091–0738					0.1181	550	2.13	12.34	HII	I
	S	00 11 43.272	–07 22 07.35	31637					...	
	N	00 11 43.302	–07 22 06.18	31686					...	
00188–0856	-	00 21 26.513	–08 39 25.99	34136	0.1285	602	2.29	12.42	Sy2	M
00509+1225	-	00 53 34.934	+12 41 35.94	17265	0.0611	273	1.18	11.87	Sy1	M
01572+0009	-	01 59 50.251	+00 23 40.88	42077	0.1633	782	2.80	12.65	Sy1	M
F05189–2524	-	05 21 01.400	–25 21 45.30	12285	0.0427	188	0.84	12.10	Sy2	M
07251–0248					0.0878	400	1.64	12.45		I
	W	07 27 37.532	–02 54 54.38	24201					HII	
	E	07 27 37.613	–02 54 54.25	24193					HII	
09022–3615	-	09 04 12.706	–36 27 01.93	16856	0.0596	266	1.15	12.33	HII	M
F10190+1322					0.0763	345	1.45	12.04		I
	W	10 21 42.493	+13 06 53.83	21336					HII	
	E	10 21 42.754	+13 06 55.61	21167					HII	
11095–0238					0.1064	491	1.95	12.33		I
	SW	11 12 03.359	–02 54 23.29	28806					LINER	
	NE	11 12 03.383	–02 54 22.94	28863					LINER	
F12072–0444					0.1284	601	2.29	12.48		I
	S	12 09 45.13	–05 01 14.6 [†]						Sy2	
	N	12 09 45.13	–05 01 13.5 [†]						Sy2	
F12112+0305					0.0730	329	1.39	12.32	LINER	I
	SW	12 13 45.940	+02 48 39.12	20448					...	
	NE	12 13 46.057	+02 48 41.55	20322					...	
13120–5453	-	13 15 06.323	–55 09 22.82	9046	0.0311	136	0.62	12.27	Sy2	M
F13451+1232					0.1217	568	2.19	12.31		I
	W	13 47 33.36	+12 17 24.2 [†]						Sy2	
	E	13 47 33.50	+12 17 23.8 [†]						LINER	
F14348–1447					0.0826	375	1.55	12.41		I
	SW	14 37 38.281	–15 00 24.23	22911					LINER	
	NE	14 37 38.397	–15 00 21.27	22809					LINER	
F14378–3651	-	14 40 59.013	–37 04 31.93	19113	0.0681	306	1.30	12.15	Sy2	M
F15327+2340					0.0181	78	0.37	12.19		M
	W	15 34 57.224	+23 30 11.44	5290					LINER	
	E	15 34 57.293	+23 30 11.29	5380					LINER	
16090–0139	-	16 11 40.419	–01 47 06.35	35352	0.1337	629	2.37	12.62	HII	M
16155+0146					0.1330	625	2.36	12.24		I
	NW	16 18 09.364	+01 39 21.75	35188					Sy2	
	SE	16 18 09.54	+01 39 19.7 [†]	
17208–0014	-	17 23 21.957	–00 17 00.88	12304	0.0428	189	0.84	12.43	LINER	M
F19297–0406					0.0856	390	1.61	12.45		I
	S	19 32 22.30	–04 00 01.8 [†]	23685					HII	
	N	19 32 22.309	–04 00 01.03	23589					HII	
19542+1110	-	19 56 35.785	+11 19 05.03	17629	0.0625	280	1.20	12.09	LINER	M
20087–0308	-	20 11 23.866	–02 59 50.72	28600	0.1055	487	1.93	12.47	LINER	M
20100–4156					0.1298	609	2.31	12.66		I
	NW	20 13 29.48	–41 47 32.6 [†]	34428					HII	
	SE	20 13 29.556	–41 47 35.21	34453					LINER	
20414–1651	-	20 44 18.159	–16 40 16.82	23962	0.0869	396	1.63	12.24	HII	M
F22491–1808					0.0776	352	1.47	12.23		I
	W	22 51 49.24	–17 52 23.7 [†]	...					HII	
	E	22 51 49.349	–17 52 24.13	21600					HII	

Notes. ^(a) Coordinates of the ~220–250 GHz continuum detected by ALMA for each nucleus (see Sect. 4.1). The typical astrometric uncertainty is 25 mas. ^(†) For the 4 nuclei undetected in the ALMA images and the 2 systems (F12072-0444 and F13451+1232) not observed by ALMA, we used near-IR and optical *HST* images, whose astrometry was tied to Gaia DR2, to measure the nuclear position (see Sect. 3.1 of Perna et al. 2021). ^(b) CO(2–1) velocity of the nucleus using the radio definition in the kinematic local standard of rest (Lamperti et al. in prep.). ^(c) Redshift using the average velocity of the system. ^(d) Luminosity distance and scale for the assumed cosmology (see Sect. 1). ^(e) 6–1500 μm IR luminosity derived from the SED fit. The typical uncertainty is 0.03 dex (see Sect. 4.3). ^(f) Nuclear activity classification based on optical spectroscopy (see Perna et al. 2021). ^(g) System morphology: I. Interacting system with nuclear separation >1 kpc; M. Advanced merger with nuclear separation <1 kpc (see Perna et al. 2021).

Table 2: Summary of the continuum ALMA observations

IRAS name	Synthesized beam (arcsec \times arcsec, $^{\circ}$) ^a	Beam FWHM ^b (pc)	Sensitivity ^c (μ Jy beam ⁻¹)	Obs freq. (GHz)	ALMA Band	ALMA Project ID
00091–0738	0.31 \times 0.23, –83	570	45	194.2	5	2018.1.00699.S
00188–0856	0.13 \times 0.12, –46	290	18	192.4	5	2018.1.00699.S
00509+1225	0.31 \times 0.28, 24	340	24	232.6	6	2018.1.00699.S
01572+0009	0.16 \times 0.13, 69	410	33	188.2	5	2018.1.00699.S
F05189–2524	0.52 \times 0.42, –70	390	34	236.7	6	2018.1.00699.S
07251–0248	0.27 \times 0.24, –50	420	23	228.3	6	2018.1.00699.S
09022–3615	0.30 \times 0.27, –87	330	24	232.9	6	2018.1.00699.S
F10190+1322	0.30 \times 0.27, 5	410	23	229.4	6	2018.1.00699.S
11095–0238	0.31 \times 0.24, –86	540	29	196.2	5	2018.1.00699.S
F12112+0305	0.30 \times 0.26, –76	390	21	231.1	6	2016.1.00170.S
13120–5453	0.65 \times 0.65, 0	400	150	239.6	6	2016.1.00777.S
F14348–1447	0.29 \times 0.25, 89	420	22	229.1	6	2016.1.00170.S
F14378–3651	0.36 \times 0.24, 84	390	41	231.1	6	2018.1.00699.S
F15327+2340	1.27 \times 0.81, 40	370	290	226.9	6	2015.1.00113.S
16090–0139	0.20 \times 0.16, –85	420	37	193.3	5	2018.1.00699.S
16155+0146	0.26 \times 0.14, –72	440	50	193.4	5	2018.1.00699.S
17208–0014	0.47 \times 0.47, 0	400	240	237.8	6	2018.1.00486.S
F19297–0406	0.27 \times 0.26, 79	420	18	228.5	6	2018.1.00699.S
19542+1110	0.35 \times 0.30, –59	390	26	232.3	6	2018.1.00699.S
20087–0308	0.31 \times 0.25, –70	540	17	196.3	5	2018.1.00699.S
20100–4156	0.18 \times 0.12, 58	350	25	193.9	5	2018.1.00699.S
20414–1651	0.18 \times 0.14, –54	260	27	228.4	6	2018.1.00699.S
F22491–1808	0.39 \times 0.29, –89	500	26	229.6	6	2015.1.00263.S

Notes. ^(a) FWHM in arcsec and east of north Position Angle in degrees of the synthesized beam. ^(b) Average beam FWHM at the distance of the system (see Table 1). ^(c) 1σ continuum sensitivity.

pipeline. The absolute flux accuracy of Band 5 and 6 data is $\sim 10\%$ (ALMA Technical Handbook). For the CO(2–1) spectral window, we subtracted a constant continuum level estimated from the line emission free channels in the uv plane. The data were cleaned using the `tclean` CASA task and the Briggs weighting with robustness parameters between -0.5 and 2.0 to match the required ~ 400 pc spatial resolution. For two systems (13120–5453 and 17208–0014), the largest synthesized beam provides a spatial resolution better than 400 pc, so we used the `imsmooth` task to convolve the cubes with a Gaussian and obtained the desired spatial resolution. For F15327+2340 (Arp 220), we only used the compact configuration data which provide a ~ 370 pc spatial resolution comparable to that of the other ULIRGs in our sample. The channel width of the final cubes is ~ 10 km s⁻¹ and the pixel sizes are about a sixth of the beam FWHM (i.e., between 20 and 120 mas). In addition to the line data cubes, we produced continuum images using spectral windows where no emission or absorption lines were present. The continuum sensitivities range from 18 to 290 μ Jy beam⁻¹ with more sensitive data for the more distant objects (see Table 2).

In this paper, we primarily focus on the analysis of the continuum and CO(2–1) maps. In a future paper (Lamperti et al. in prep.), we will present the detailed analysis of the line data.

3.2. Ancillary *Spitzer* data

To complete the spectral energy distribution (SED) of the ULIRGs (Sect. 4.3), we used mid-IR *Spitzer* data. In particular we used the 5.2–38 μ m low-resolution ($R \sim 60 - 130$) spectra from the Infrared Spectrograph (IRS; Houck et al. 2004) and the 70 and 160 μ m images from the Multiband Imaging Photometer (MIPS; Rieke et al. 2004).

We downloaded the calibrated IRS spectra for all the systems in our sample from the Cornell Atlas of *Spitzer*/Infrared Spectrograph Sources (CASSIS; Lebouteiller et al. 2011) and measured the flux at 34 μ m, which is approximately at the middle point between the 24 and 70 μ m photometric points in log scale and avoids the noisier long-wavelength edge of the IRS spectrum.

We also downloaded the calibrated MIPS images for 5 systems from the *Spitzer* Heritage Archive¹. The ULIRG systems appear as point-sources at the MIPS angular resolution (18'' and 40'' at 70 and 160 μ m, respectively). For the 70 μ m image, we used a 35'' radius aperture and a 39–65'' background annulus and then multiplied the flux by 1.24 to account for the aperture correction factor (see Table 4.14 of the MIPS Instrument Handbook). For the 160 μ m images, we subtracted a global background emission level and used a 60'' radius aperture. We applied a 1.40 aperture correction factor which is appropriate for sources with temperatures between 30 and 150 K (see Table 4.15 of the MIPS Instrument Handbook). The measured *Spitzer* IRS and MIPS fluxes are listed in Appendix A.

4. Data analysis

4.1. ALMA continuum model. Size and flux

We modeled the ALMA 220–250 GHz continuum images to determine the flux, size, and position of the detected emitting regions. In general, these regions are compact (FWHMs similar to the beam size) and their morphological structure is barely resolved. Therefore, we used simple models consisting of a point-source, a Gaussian, point-source + Gaussian, or 2 Gaussians. These models were convolved with the beam and compared with the observations to determine a χ^2 value. Then, we minimized

¹ <https://sha.ipac.caltech.edu>

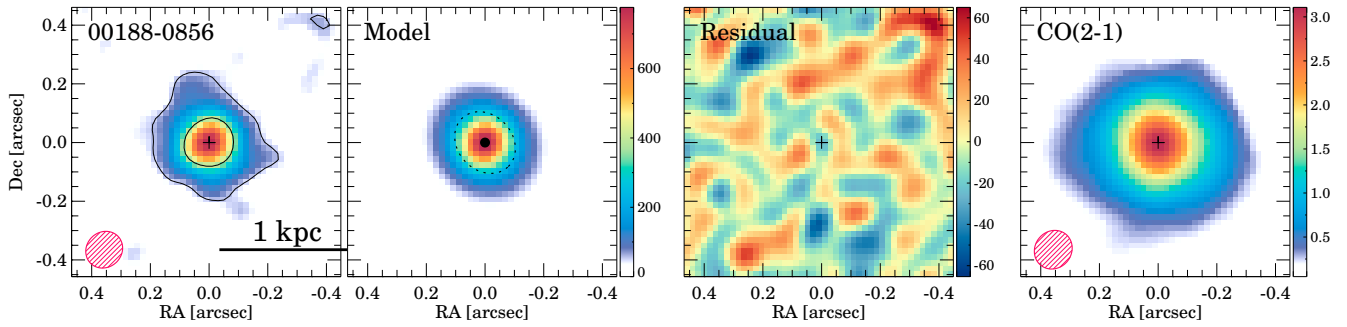


Fig. 1: ALMA continuum observation (first panel), best-fit model (second panel), residual emission after subtracting the continuum model (third panel), and the integrated CO(2–1) emission (moment 0) from Lamperti et al. in prep. (fourth panel) for 00188–0856 as an example. The two contour levels in the first panel indicate the 3σ and the $0.5\times$ peak emission levels. In the second panel, the individual components of the best-fit model are presented as a black circle (point source model) and as a dashed ellipse (deconvolved Gaussian model). The black crosses in the first, third, and fourth panels mark the fitted location of the continuum peak. The red hatched ellipses represent the beam FWHM. The units are $\mu\text{Jy beam}^{-1}$ for the continuum panels and $\text{Jy km s}^{-1} \text{ beam}^{-1}$ for the CO(2–1) panel. The continuum model fits for the whole sample are shown in Fig. B.1.

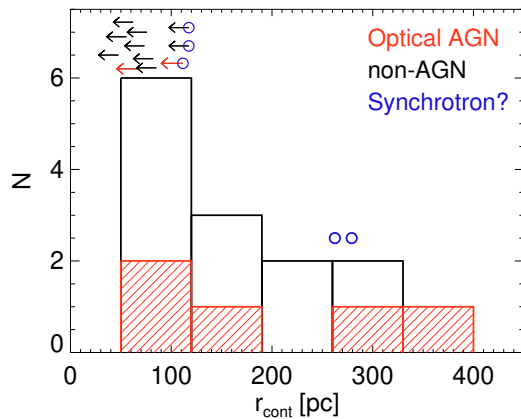


Fig. 2: Distribution of the ~ 220 GHz continuum half-light radius (r_{cont} ; see Table 3). Upper limits are indicated with arrows. The red (black) histogram bars and arrows correspond to galaxies classified as AGN (non-AGN) from optical spectroscopy. The sizes of the systems whose ALMA flux might have high ($>40\%$) non-thermal synchrotron contributions are marked in blue (see Sect. 5.1.2).

the χ^2 by varying the fluxes, sizes, and positions of the model components.

We tried these 4 models for each nucleus and selected that with the lowest reduced χ^2 . The best-fit models reproduce quite well the observed emission. The median (mean) reduced χ^2 is 1.1 (1.4), the maximum is 3.1, and no significant structures are seen in the residual images (see Fig. 1). This figure also shows the best-fit model whose parameters are listed in Table 3. The best-fit positions are presented in Table 1. Based on these parameters, we computed the half-light radius of the ~ 220 GHz continuum, r_{cont} , which is defined as the radius of the region that contains 50% of the observed flux.

For 11 nuclei whose model includes a point-source, the half-light radius is not well defined because the point source contributes $>50\%$ to the total flux. Therefore, to estimate the size upper limit in these cases, we performed a series of simulations. First, we subtracted, when present, the extended Gaussian component of the model. Then, we used circular Gaussian models

with fixed FWHM from 2 to 6 pixels², that were convolved with the beam, and obtained the χ^2 variation as function of the model FWHM. Finally, we estimated the 3σ FWHM upper limit as the FWHM at which the χ^2 increases by 9.0³ with respect to the minimum χ^2 . The FWHM upper limits are also included in Table 3.

Fig. 2 shows the distribution of the half-light radius and the upper limits. The measured r_{cont} range from <50 pc to 350 pc with a median value of 80–100 pc. The r_{cont} of AGN and non-AGN objects, based on optical spectroscopy, are similar.

Mid-IR observations already indicate that ULIRGs are very compact (<1 kpc; Soifer et al. 2000; Díaz-Santos et al. 2010; Alonso-Herrero et al. 2014, 2016; Imanishi et al. 2020). Our higher angular resolution ALMA continuum data suggest that they are even more compact.

4.1.1. Higher resolution observations

The CO(2–1) and 230 GHz continuum emission of F15327+2340 (Arp 220) have been observed by ALMA at much higher resolution (8 pc) than the data used in this paper. However, these data are still unpublished. Instead, we can compare with the 20–40 pc 2.7 mm (~ 110 GHz) continuum observations presented by Scoville et al. (2017) and Sakamoto et al. (2017). These authors measure deconvolved Gaussian FWHM of 160–180 mas for the East nucleus and 74–114 mas for the West nucleus. From the low resolution data, we obtained $2\times r_{\text{cont}}=400$ mas and <260 mas for the East and West nuclei, respectively. Therefore, we recover a reliable upper limit size for the bright and compact source in the West nucleus. For the East nucleus, we derive a size 2 times larger. However, it is possible that part of extended emission detected in the low-resolution data is filtered out, or too faint, in the ten times higher resolution published observations.

In addition, 17208–0014 was observed as part of another program which aimed to obtain ~ 100 pc spatial resolution CO(2–1) and continuum data. These observations will be analyzed in detail in a future paper. However, here we use the high

² 6 pixels approximately corresponds to the beam FWHM.

³ The 9.0 constant corresponds to the value at which the cumulative distribution function of a χ^2 distribution with one degree of freedom is equivalent to a 3σ confidence interval of a normal distribution (~ 0.997).

Table 3: ALMA continuum models

IRAS name	Nucleus	Rest freq. (GHz)	Total flux ^a (mJy)	Point Flux (mJy)	Flux (mJy)	Gaussian 1 FWHM ^b (mas, mas)	Flux (mJy)	Gaussian 2 FWHM ^b (mas, mas)	r_{cont}^c (mas)	(pc)	χ^2_{red}
00091-0738	S	217.10	4.83±0.05	4.83±0.05	<40	<85	0.91
	N		<0.15
00188-0856	-	217.12	1.74±0.10	0.47±0.03	1.26±0.09	227±24,187±13	75±2	173	0.98
00509+1225	-	246.83	1.03±0.07	...	1.03±0.07	191±20,104±22	70±4	83	1.05
01572+0009	-	218.90	1.12±0.13	0.53±0.05	0.59±0.11	331±100,89±70	22±4	63	1.05
F05189-2524	-	246.86	6.29±0.21	3.90±0.12	2.39±0.18	488±42,449±24	<80	<67	1.13
07251-0248	W	248.39	0.97±0.05	...	0.97±0.05	122±16,95±18	53±3	88	0.73
	E		9.29±0.15	7.74±0.14	1.55±0.07	328±51,199±21	<50	<82	1.20
09022-3615	-	246.80	6.98±0.59	...	2.50±0.32	319±107,18±93	4.48±1.05	1050±160,540±133	227±66	262	2.17
F10190+1322	W	246.86	0.39±0.10	...	0.39±0.10	483±133,258±104	176±22	255	1.01
	E		2.80±0.11	0.79±0.06	2.00±0.09	618±37,294±26	153±4	222	1.25
11095-0238	SW	217.13	0.41±0.13	...	0.41±0.13	275±112,48±76	<60	<117	1.11
	NE		0.89±0.03	0.89±0.03	<60	<117	1.11
F12112+0305	SW	247.99	0.70±0.09	0.13±0.04	0.57±0.08	273±93,178±64	93±11	129	0.73
	NE		6.84±0.11	4.78±0.07	2.06±0.08	430±22,369±24	<40	<55	1.13
13120-5453	-	247.05	32.14±2.23	...	15.04±1.16	668±143,518±115	17.09±1.37	1504±223,1328±196	448±89	279	1.03
F14348-1447	SW	248.00	2.82±0.11	1.51±0.04	1.31±0.10	601±75,482±44	<40	<62	0.96
	NE		1.69±0.13	0.71±0.11	0.98±0.06	326±49,239±28	64±3	100	1.07
F14378-3651	-	246.84	2.66±0.18	0.48±0.07	2.18±0.16	714±54,540±34	262±6	342	1.12
F15327+2340	W	230.98	135.50±1.48	117.36±0.97	18.13±1.11	1739±205,1119±181	<130	<47	1.22
	E		56.16±1.03	...	56.16±1.03	509±34,357±20	213±5	78	...
16090-0139	-	219.09	3.11±0.19	0.38±0.13	2.73±0.13	355±35,186±28	116±4	275	1.37
16155+0146	NW	219.14	0.60±0.08	0.60±0.08	<47	<111	0.87
	SE		<0.15
17208-0014	-	247.99	42.60±1.12	20.45±0.56	22.15±0.97	842±58,636±44	<90	<75	1.33
F19297-0406	S	248.01	<0.06
	N		5.99±0.45	...	3.40±0.28	247±15,83±13	2.58±0.34	718±82,640±76	113±4	182	2.74
19542+1110	-	246.81	3.50±0.21	1.28±0.12	2.22±0.19	354±32,276±33	91±3	110	1.05
20087-0308	-	217.05	5.56±0.14	2.47±0.07	3.09±0.12	457±19,332±12	78±2	151	2.11
20100-4156	NW	219.11	<0.08
	SE		3.74±0.21	1.66±0.15	2.08±0.14	211±26,152±15	34±2	80	2.39
20414-1651	-	248.28	4.57±0.44	1.82±0.30	2.75±0.32	191±45,131±38	41±4	66	3.10
F22491-1808	W	247.48	<0.08
	E		5.08±0.26	3.90±0.14	1.17±0.22	628±196,383±44	<50	<73	2.89

Notes. In addition to the statistical uncertainties listed in this table, the absolute flux accuracy is ~10%. ^(a) Total flux including all the model components (point source, Gaussian 1, and Gaussian 2). For undetected sources, we indicate the 3 σ upper limit. ^(b) Deconvolved FWHM of the Gaussian models. ^(c) Deconvolved half-light radius.

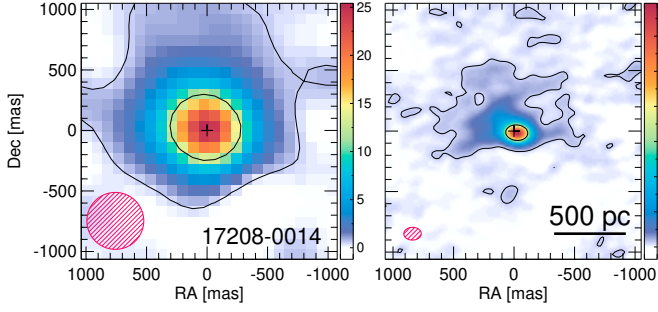


Fig. 3: Comparison between the 400 pc resolution 247 GHz continuum image analyzed in Sect. 4.1 (left panel) and the higher resolution (120 pc) data (right panel) available for 17208–0014. The black cross is the position of the center measured on the 400 pc image. The contours are as in Fig. 1. The hatched red ellipses correspond to the beam FWHM of each image. The color scales are in mJy beam^{-1} .

resolution continuum data (120 pc vs. 400 pc), to test whether the source size derived from the low-resolution data ($r_{\text{cont}} < 75$ pc for this object) is consistent with the size measured in the high-resolution data.

Fig. 3 compares the low- and the high-resolution maps. The difference between the continuum fluxes in both images measured using a $1''$ radius aperture is $< 9\%$ (42.7 ± 0.2 vs. 46.3 ± 0.3 mJy). This indicates that the higher resolution data do not miss significant low surface brightness emission. This figure also shows that the continuum emission peak measured in the original low-resolution data (Table 1) appears slightly shifted (30 mas or 26 pc) in the high-resolution image. This is possibly because now we start to spatially resolve the inner structure of the nucleus and multiple smaller regions appear.

We applied the same model fitting procedure described in Sect. 4.1 to the higher resolution image. The original model consisted of a point source plus a Gaussian (see Table 3 and Fig. B.1). For the high-resolution data, we used 2 Gaussians since the emission core is resolved. This “core” Gaussian has a flux of 17.6 ± 1.1 mJy and a circularized FWHM of 74 ± 3 mas (62 pc; $r_{\text{cont}} = 31$ pc). It contains about 40% of the 247 GHz continuum emission from 17208–0014, so the $r_{\text{cont}} < 75$ pc upper limit we estimated from the low-resolution data (Table 3) seems to be consistent with what is observed at higher angular resolution.

The result for these two objects supports that our method to estimate the r_{cont} can produce realistic values, even below the beam size.

4.2. Nuclear molecular gas

Figs. 1 and B.1 show that the CO(2–1) emission is more extended than the continuum and also that it has a more complex morphology. As a consequence, the simple set of models used to fit the continuum (Sect. 4.1) does not reproduce the CO(2–1) emission properly. Therefore, we considered a different approach to determine the size and flux of the nuclear CO(2–1) emission.

We used the CO(2–1) moment 0 maps (Lamperti et al. in prep.) to extract the flux in concentric apertures centered at the continuum peak. This produces an azimuthally averaged growth curve for the CO(2–1) emission (see Fig. 4). To fit this curve,

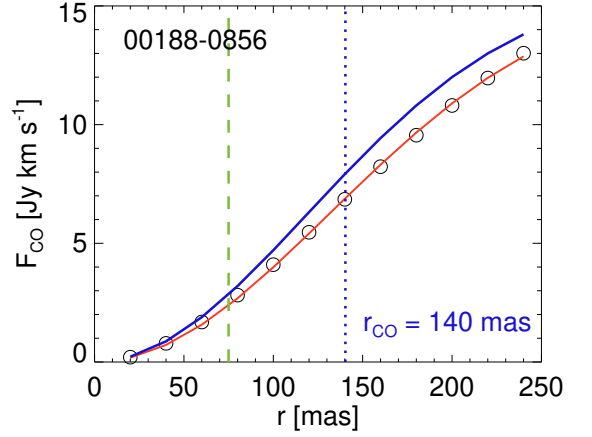


Fig. 4: Growth curve of the CO(2–1) moment 0 map for 00188–0856 as an example. The circles correspond to the observed flux within a circular aperture of radius r . The red line is the best fit model (Sect. 4.2). The deconvolved best fit profile is shown in blue and its effective radius, $r_{\text{CO}} = \text{FWHM}/2$, is indicated by the vertical blue dotted line. The dashed green line marks the ~ 220 GHz continuum radius, r_{cont} for comparison. The CO(2–1) model fits for the whole sample are shown in Fig. C.1.

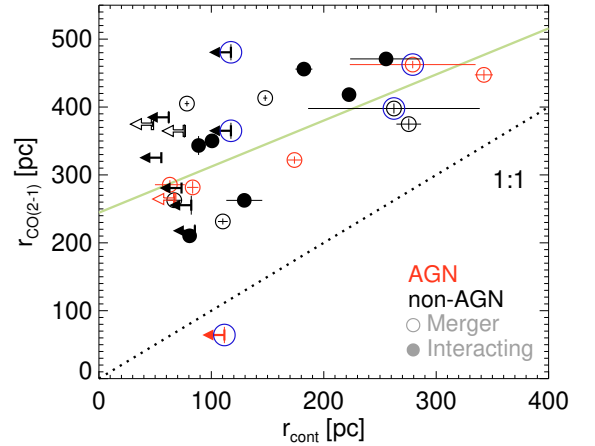


Fig. 5: Half light radius of the 220 GHz continuum r_{cont} vs. $0.5 \times \text{FWHM}$ of the CO(2–1) emission r_{CO} . Red (black) symbols mark systems classified as AGN (non-AGN) based on optical spectroscopy. Filled symbols correspond to nuclei in interacting systems and empty symbols of nuclei in mergers (see Table 1). Blue encircled symbols are galaxies with excess non-thermal emission whose continuum size estimates might be inaccurate (Sect. 5.1.2). The green line is best linear fit excluding the nuclei with r_{cont} upper limits. The dotted line indicates the 1:1 relation.

we simulated a 2D circular Gaussian model, which was convolved with the beam, and we compared the model growth curve with the observed one. From this fit, we obtained the deconvolved circularized FWHM of the CO(2–1) emission and the nuclear flux. Then, we used a ULIRG-like α_{CO} conversion factor ($0.78 M_{\odot} (\text{K km s}^{-1} \text{ pc}^{-2})^{-1}$) and a CO 2–1 to 1–0 ratio $r_{21} = 0.91$ (Bolatto et al. 2013) to estimate the molecular gas mass. We limited this growth curve to the central ~ 1.5 kpc, so the most

Table 4: Nuclear CO(2–1) emission and cold molecular gas mass

IRAS name	Nucleus	r_{CO}^a (pc)	S_{CO}^b (Jy km s ⁻¹)	$\log M_{\text{H}_2}^c$ (M_\odot)	$\log \Sigma_{\text{H}_2}^d$ ($M_\odot \text{ pc}^{-2}$)
00091–0738	S	217±9	11.6±0.1	9.22±0.04	3.74±0.05
	N	421±9	8.00±0.41	9.05±0.05	3.01±0.06
00188–0856	-	321±5	15.9±0.2	9.43±0.04	3.61±0.05
00509+1225	-	281±9	22.7±0.4	8.92±0.04	3.23±0.06
01572+0009	-	285±6	5.12±0.07	9.15±0.04	3.44±0.04
F05189–2524	-	264±8	71.3±0.9	9.11±0.04	3.46±0.06
07251–0248	W	343±13	12.5±1.7	8.99±0.07	3.12±0.09
	E	255±13	31.7±0.4	9.39±0.04	3.78±0.06
09022–3615	-	397±7	153±2	9.73±0.04	3.74±0.04
F10190+1322	W	470±9	17.0±0.8	9.00±0.05	2.85±0.05
	E	418±9	52.6±0.8	9.49±0.04	3.44±0.05
11095–0238	SW	480±11	20.1±0.8	9.36±0.05	3.20±0.05
	NE	365±11	22.5±0.5	9.41±0.04	3.49±0.05
F12112+0305	SW	262±6	17.2±0.5	8.96±0.05	3.33±0.05
	NE	325±6	72.2±0.9	9.58±0.04	3.76±0.05
13120–5453	-	462±5	472±5	9.65±0.04	3.52±0.05
F14348–1447	SW	384±9	53.9±0.8	9.57±0.04	3.60±0.04
	NE	350±9	33.3±1.3	9.36±0.05	3.47±0.05
F14378–3651	-	447±7	40.9±0.6	9.28±0.04	3.18±0.05
F15327+2340 [†]	-	370±4	1360±7	9.63±0.04	3.69±0.05
16090–0139	-	374±8	43.9±0.6	9.91±0.04	3.96±0.06
16155+0146	NW	64±12	2.24±0.03	8.61±0.04	4.19±0.16
	SE	...	<0.04	<6.81	...
17208–0014	-	364±9	338±6	9.79±0.04	3.86±0.05
F19297–0406	S	...	1.2±0.3	7.93±0.11	...
	N	455±8	81.7±1.3	9.78±0.04	3.66±0.05
19542+1110	-	231±4	35.4±0.2	9.14±0.04	3.61±0.04
20087–0308	-	413±4	59.7±0.6	9.83±0.04	3.80±0.05
20100–4156	NW	364±8	0.939±0.042	8.21±0.05	2.29±0.05
	SE	210±4	21.1±0.1	9.56±0.04	4.12±0.05
20414–1651	-	262±5	32.2±0.5	9.39±0.04	3.75±0.06
F22491–1808	W	...	0.41±0.02	7.38±0.02	...
	E	280±5	45.4±0.3	9.44±0.04	3.74±0.05

Notes. ^(a) Deconvolved radius ($0.5 \times \text{FWHM}$) of the nuclear CO(2–1) Gaussian emission model. ^(b) Nuclear CO(2–1) flux derived from the Gaussian model. This value does not include extended CO(2–1) emission beyond $r > 0.7$ kpc. In addition to the statistical uncertainties listed in this column, the absolute flux accuracy is $\sim 10\%$. ^(c) Molecular gas mass calculated using a ULIRG-like α_{CO} conversion factor ($0.78 M_\odot (\text{K km s}^{-1} \text{ pc}^{-2})^{-1}$) and a CO 2–1 to 1–0 ratio $r_{21} = 0.91$ (see Sect. 4.2). ^(d) CO(2–1) surface density within r_{CO} calculated as $0.5 \times M_{\text{H}_2} / (\pi r_{\text{CO}}^2)$. ^(†) At the resolution of these observations (370 pc) it is not possible to disentangle the CO(2–1) emission from the two nuclei of F15327+2340 (see Fig. B.1).

extended emission of the systems is not included in the measured flux. Nevertheless, we are mostly interested in the CO(2–1) sizes and fluxes of the nuclear regions detected in the continuum and these are well covered by the apertures used (~ 700 pc aperture radius vs. $r_{\text{cont}} < 350$ pc). The nuclear CO(2–1) deconvolved sizes, r_{CO} , fluxes, molecular gas masses, and molecular gas surface densities, Σ_{H_2} , are presented in Table 4.

The CO(2–1) radius r_{CO} ranges from 60 to 500 pc (median 320 pc). Fig. 5 shows that r_{CO} is larger than the continuum size r_{cont} . The median $r_{\text{CO}}/r_{\text{cont}}$ ratio is 2.5 ± 1.1 . As for the continuum size, we do not find significant differences between the r_{CO} of AGN and non-AGN nuclei. If we exclude the nuclei with upper limits for r_{cont} , there is a good correlation between the CO and continuum sizes (Spearman’s rank correlation coefficient $r_s = 0.72$, probability of no correlation $p = 7 \times 10^{-4}$). The best linear fit is $r_{\text{CO}} = (0.70 \pm 15) \times r_{\text{cont}} + (240 \pm 30)$ pc.

4.3. Spectral energy distribution fit

4.3.1. Infrared SED

We fitted the IR spectral energy distribution of these ULIRGs to determine the expected dust emission at the ALMA frequency (220–250 GHz \approx 1400–1200 μm). We used published IR photometry from *Herschel*, *ISO*, and *IRAS* (see Table 5), as well as *Spitzer* IRS and MIPS data (see Sect. 3.2 and Appendix A). For observation at similar wavelengths, we gave preference to the data with the highest angular resolution.

We fitted the far-IR SED using a single-temperature graybody (e.g., equations 1 and 2 of Kovács et al. 2010). We assumed a fixed $\beta = 1.8$ (Planck Collaboration et al. 2011), but allowed the optical depth to vary. This model reproduces well the observed far-IR SED between 30 and 500 μm for most objects. At shorter wavelengths, some of these ULIRGs have excess mid-IR emission which has been associated with warmer dust due to an AGN (e.g., Nardini et al. 2009; Veilleux et al. 2009). Since we are interested in the longer wavelength emission to compare with the ALMA observation, we only used in the fit the photometric points between 34 and 500 μm to avoid any bias due to

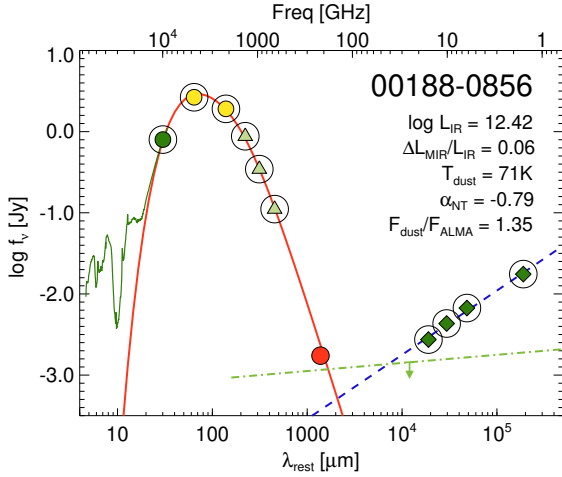


Fig. 6: SED fit for 00188–0856 as an example. The data points correspond to the radio (green diamonds), ALMA ~ 220 GHz from this paper (red circle), and IR (remaining points) observations. The solid green line is the 5–38 μm *Spitzer*/IRS spectrum. The IR observations are color coded as follows: *Spitzer*/IRS synthetic photometry at 34 μm (green circle); *Spitzer*/MIPS (yellow circles); and *Herschel*/SPIRE (green triangles). The solid red line is the best gray-body fit and the dashed blue line represents the best power-law fit to the non-thermal radio emission. Only the encircled symbols have been used for the fits (i.e., the ALMA point is excluded from the SED fit). The dot-dashed green line represents the expected maximum free-free emission assuming that all the L_{IR} is produced by SF (see Sect. 4.3). The SED fits for the whole sample are shown in Fig. D.1.

this mid-IR excess. We note that we excluded the ALMA continuum flux from the SED fit. For four systems (00509+1225, 01572+0009, F05189-2524, and F13451+1232), we started the fit at 70 μm because the excess mid-IR emission was clear even at the 34 μm photometric point. Also, for F13451+1232 (which hosts the radio source 4C+12.50), we excluded the 500 μm flux because it has a noticeable contribution from non-thermal emission. We show the best-fit models in Figs. 6 and D.1 and the model parameters are presented in Table 6. To compute the total IR luminosity between 6 and 1500 μm (rest-frame), we first integrated the gray body emission. Then we subtracted the gray body model to the IRS spectrum and obtained the 6–20 μm mid-IR excess, $\Delta L_{6-20\mu\text{m}}$. The total L_{IR} is the addition of the gray body emission and the mid-IR excess. The total L_{IR} and the $\Delta L_{6-20\mu\text{m}}/L_{\text{IR}}$ ratio are listed in Tables 1 and 6, respectively.

4.3.2. Non-thermal synchrotron emission

At the frequency of the ALMA observations, it is possible to have a significant contribution from non-thermal synchrotron emission. To estimate this contribution, we used published radio observations of our sample of ULIRGs with frequencies between 1 and 40 GHz (Table 5). All the systems have been observed at least at 1.4 GHz, except 13120–5453 which only has 4.85 and 0.843 GHz data. For objects with more than one radio observation (16 systems), we fitted a power law to the radio data. We obtained spectral indexes between -0.3 and -1.0 with a mean index of -0.62 (see Table 6), which are similar to the spectral indexes found in a sample of 31 local ULIRGs by Clemens et al. (2008). For the remaining objects with just one

Table 5: Far-IR and radio fluxes references

IRAS name	IR	Radio
00091–0738	M90	H15, H21
00188–0856	PS21, P16	H15, H21
00509+1225	P15	H15, B89
01572+0009	P15, P16	H15, B89
F05189–2524	P16, C17	C90, C91
07251–0248	C17	C98
09022–3615	P16, C17	C98
F10190+1322	M90, PS21	H15
11095–0238	P16, PS21	H15
F12072–0444	M90, P16	H15
F12112+0305	C17	C90, C91
13120–5453	P16, C17	W94, M07
F13451+1232	PS21	S98
F14348–1447	P16, C17	C90, C91
F14378–3651	P16, C17	C98, M03
F15327+2340	M90, C17	C91, C98, BM15
16090–0139	M90, K01, P16	C98
16155+0146	M90	H15
17208–0014	P16, C17	B06
F19297–0406	P16, C17	C98
19542+1110	C17	C98, L11
20087–0308	M90, P16	W98, C98, M17
20100–4156	PS21, P16	C96
20414–1651	M90, P16	C98, N03
F22491–1808	P16, C17	C90, C91, H21

References. IR: (C17) Chu et al. 2017; (K01) Klaas et al. 2001; (M90) Moshir & et al. 1990; (P15) Petric et al. 2015; (P16) Pearson et al. 2016; (S03) Sanders et al. 2003; and (PS21) this work Appendix A. Radio: (B89) Barvainis & Antonucci 1989; (B06) Baan & Klöckner 2006; (BM15) Barcos-Muñoz et al. 2015; (C90) Condon et al. 1990; (C91) Condon et al. 1991; (C96) Condon et al. 1996; (C98) Condon et al. 1998; (H15) Helfand et al. 2015; (H21) Hayashi et al. 2021; (L11) Leroy et al. 2011; (M03) Mauch et al. 2003; (M07) Murphy et al. 2007; (M17) Meyers et al. 2017; (N03) Nagar et al. 2003; (S98) Stanghellini et al. 1998; and (W94) Wright et al. 1994;

radio observation at 1.4 GHz (9 systems), we assumed the mean spectral index between 1.4 and 22.5 GHz ($\alpha_{22.5}^{1.4} = -0.671$) measured in local ULIRGs (Clemens et al. 2008). We find that the non-thermal emission contributes between 4 and 55% (median 20%) of the ALMA continuum flux (Table 6). In this fit, we ignored that the free-free emission (see below) can also affect (flatten) the spectral index (e.g., Hayashi et al. 2021). Therefore, if the free-free emission is strong compared to the synchrotron, our “non-thermal” contribution estimate would be closer to the combined free-free+synchrotron total emission.

For 20087–0308, the predicted non-thermal flux is 2.8 times higher than the observed ALMA flux. However, this source shows radio fluxes between 1.4 and 4.85 GHz that are not fully compatible with a power-law (Fig. D.1). This suggests that either the power-law model is not adequate for this source, that it presents variable radio emission, or that some of the radio fluxes are not reliable.

4.3.3. Free-free thermal emission

The ALMA continuum measurements can also include a contribution from thermal free-free emission. The free-free emission is related to the ionizing photon rate from young stars and can trace the SFR (e.g., Condon & Ransom 2016). We used the relation between the SFR and the free-free radio emission to estimate its

contribution at the ALMA frequency (equation 11 from [Murphy et al. 2011](#)). The SFR of the ULIRGs was derived from the total IR luminosity using the [Kennicutt & Evans \(2012\)](#) calibration. The free-free contributions are presented in Table 6. However, we note that this free-free emission estimate is an upper limit because we ignored the potential AGN contribution to the L_{IR} , and also because, in the dusty nuclear regions of ULIRGs, a fraction of the ionizing photons can be absorbed by dust grains instead of ionizing H atoms and, therefore, reduce the actual free-free emission (e.g., [Abel et al. 2009](#)). Actually, with these assumptions, six systems (five classified as AGN and one as LINER) have predicted free-free upper limits above 90–100% of the observed ALMA flux. This indicates that a large part of their L_{IR} likely comes from an AGN and it cannot be directly translated into SFR and subsequently into free-free emission.

5. Discussion

5.1. ALMA continuum as tracer of the IR luminosity

We aim to determine the physical size and luminosity surface density of the regions that emit the bulk of the IR luminosity in local ULIRGs. Far-infrared telescopes, that detect the peak of the IR emission, lack the angular resolution to spatially resolve it, although it is possible to infer the size of the far-IR emission through indirect methods like the modeling of far-IR OH absorptions (e.g., [González-Alfonso et al. 2015](#)). In this section, we investigate if the ~ 220 GHz ALMA continuum, which provides much higher angular resolutions, can be used as a proxy of the IR emission to obtain direct estimates of the IR emitting region sizes.

However, using the ~ 220 GHz continuum to trace the size of ULIRGs is not straightforward. At this frequency, the continuum includes emission from dust, which is connected to the IR luminosity, but it may also include contributions from free-free and synchrotron emissions ([Condon & Ransom 2016](#)), which might not be directly related to the IR luminosity. This is important because, even if the IR luminosity of local ULIRGs is thought to be dominated by SF, the AGN contribution increases with increasing L_{IR} ([Veilleux et al. 2009](#); [Nardini et al. 2009](#)), and the synchrotron AGN emission could affect the ~ 220 GHz source sizes. In addition, ALMA is an interferometer, so part of the emission might be filtered out. In this section, we study the impact of these effects on the measured source sizes.

5.1.1. Filtered out flux

In general, due to the limited coverage of the uv plane, interferometric observations filter out extended large scale emission. Therefore, it might be possible that extended continuum emission from our ULIRGs is missing in the measured fluxes (Sect. 4.1). To evaluate this possibility we compare the maximum recoverable scale of our observations (about 4 kpc; Sect. 3.1) with the sizes of the detected sources. The radii range from <60 to 300 pc (Sect. 4.1 and Table 3), which are $\ll 4$ kpc. If >4 kpc structures were actually present in these ULIRGs, we would expect to detect, in addition to these very compact sources, intermediate size structures (~ 2 kpc FWHM) which are not seen in the continuum images. This suggests that the 220 GHz continuum of ULIRGs is intrinsically compact and that we can recover most of the continuum emission with these data.

It also possible that we do not detect extended low-surface brightness continuum emission due to the observations sensitivity. To quantify its possible impact, we assume an emitting area

with a 4×4 kpc² size (the typical H α effective radius of ULIRGs is <2 kpc; [Arribas et al. 2012](#)). From the continuum sensitivity, Table 2, we estimated extended emission 3σ upper limits which are on average 8% of the measured fluxes and up to 20–75% for the 4 faint nuclei with $f_{220\text{GHz}} < 0.7$ mJy (F10190+1322 W; 11095–0238 SW, F12112+0305 SW, and 16155+0146 NW; see Table 3). Therefore, if low-surface brightness emission is present, its contribution would be small for the great majority of the nuclei (at least for 25 out of 29).

5.1.2. Dust, free-free, and synchrotron contributions

At the frequencies of the ALMA observations (190–250 GHz), in addition to the Rayleigh-Jeans tail of the IR dust emission, a contribution from thermal free-free, and non-thermal synchrotron emission is possible. In particular, we explore whether the free-free or synchrotron emissions could bias the measured sizes toward more compact sizes in the case of a starburst nucleus.

Dust We first estimate the dust contribution. Based on the IR SED modeling (Sect. 4.3), we found that the ALMA flux densities are just slightly lower than the extrapolation of the IR gray-body fit (median ratio of 1.14; Table 6). We note that we did not use the ALMA flux in the gray-body fit. Thus, a possible interpretation for the good agreement between the data and the model prediction is that the ALMA flux comes from the long-wavelength tail of the dust gray-body emission. If this is the case, we could use the high-resolution ALMA data to determine the size of the IR emitting regions. This good agreement between the ALMA continuum flux and the IR SED extrapolation was also found by [Imanishi et al. \(2019\)](#) using 260 GHz observations of local ULIRGs at comparable spatial resolutions.

Free-Free The ALMA emission can include free-free emission as well. The free-free emission is produced by ionized hydrogen usually associated with star-forming regions (see Sect. 4.3.1). We estimated an upper limit for the free-free emission assuming that all the L_{IR} is produced by SF (i.e., ignoring the possible AGN contribution). This assumption also implies that dust does not absorb any ionizing photon (Sect. 4.3.1). The upper limit for the free-free contribution has a median value of $<65\%$ (Table 6). But even if the free-free emission dominates the ALMA flux, it should not affect the region size estimates since, for this free-free upper limit estimation, both IR and free-free emissions should be co-spatial as they have a common star-formation origin. Moreover, taking into account the AGN contribution to the L_{IR} and the effect of absorption of UV photons by dust would reduce this upper limit and, therefore, the possible impact of the free-free emission on the source size measurements.

Synchrotron Some contribution from synchrotron emission is possible too. If this synchrotron emission is produced by supernovae (i.e., related to star-forming regions), the ALMA regions sizes should not be affected since the IR emission and the supernovae (SNe) should have similar spatial distributions. Alternatively, AGN can produce strong synchrotron emission. In our sample, only F13451+1232 (4C+12.50) has excess radio emission with respect to the radio-IR relation (see [Perna et al. 2021](#)). Actually, the F13451+1232 ~ 220 GHz emission is dominated by synchrotron radiation (see Fig. D.1) and, therefore, cannot be directly used as a proxy of the IR emitting region. For the remain-

Table 6: IR and radio SED fit results

IRAS name	$T_{\text{dust}}/\text{K}^a$	$\tau_{350\mu\text{m}}^b$	$\log \Delta L_{6-20\mu\text{m}}/L_{\text{IR}}$	$\alpha_{\text{non-thermal}}^c$	$F_{\text{dust}}/F_{\text{ALMA}}^d$	$F_{\text{free-free}}/F_{\text{ALMA}}^d$	$F_{\text{non-thermal}}/F_{\text{ALMA}}^d$
00091–0738	78	0.40	-1.45 ± 0.19	-0.33 ± 0.05	0.22 ± 0.04	<0.24	0.20 ± 0.03
00188–0856	71	0.71 ± 0.09	-1.23 ± 0.10	-0.79 ± 0.05	1.35 ± 0.14	<0.67	0.21 ± 0.05
00509+1225	57	0.66 ± 0.17	-0.34 ± 0.01	-0.68 ± 0.05	4.39 ± 0.56	<1.77	0.16 ± 0.03
01572+0009	77	0.42 ± 0.17	-0.73 ± 0.11	-1.02 ± 0.05	0.90 ± 0.08	<1.16	0.15 ± 0.04
F05189–2524	66	0.28 ± 0.17	-0.72 ± 0.10	-0.54 ± 0.10	1.31 ± 0.10	<0.99	0.28 ± 0.12
07251–0248	75	0.50 ± 0.08	-1.54 ± 0.25	-0.671	0.61 ± 0.06	<0.27	0.04
09022–3615	65	0.30 ± 0.04	-1.10 ± 0.06	-0.671	1.39 ± 0.10	<0.70	0.40
F10190+1322	61	0.40	-1.33 ± 0.06	-0.671	1.49 ± 0.18	<0.46	0.17
11095–0238	85	0.27 ± 0.05	-1.26 ± 0.20	-0.671	0.53 ± 0.04	<1.06	0.55
F12072–0444	82	0.36 ± 0.06	-0.93 ± 0.08	-0.671
F12112+0305	63	0.36 ± 0.05	-1.63 ± 0.16	-0.51 ± 0.07	1.14 ± 0.09	<0.41	0.23 ± 0.07
13120–5453	58	0.37 ± 0.05	-1.45 ± 0.07	-0.63 ± 0.05	1.82 ± 0.15	<0.50	0.38 ± 0.10
F13451+1232	70	0.64 ± 0.24	-0.66 ± 0.05	-0.54 ± 0.03
F14348–1447	64	0.35 ± 0.04	-1.62 ± 0.14	-0.75 ± 0.06	1.62 ± 0.12	<0.65	0.17 ± 0.06
F14378–3651	66	0.32 ± 0.05	-1.48 ± 0.18	-1.00 ± 0.25	1.95 ± 0.14	<0.91	0.08 ± 0.10
F15327+2340	63	0.57 ± 0.10	-1.86 ± 0.24	-0.53 ± 0.05	0.73 ± 0.06	<0.26	0.13 ± 0.02
16090–0139	69	0.39 ± 0.05	-1.31 ± 0.08	-0.671	0.70 ± 0.05	<0.54	0.25
16155+0146	95	0.40	-0.86 ± 0.13	-0.671	0.56 ± 0.05	<1.20	0.49
17208–0014	62	0.38 ± 0.06	-1.73 ± 0.17	-0.47 ± 0.09	0.89 ± 0.08	<0.28	0.20 ± 0.06
F19297–0406	67	0.48 ± 0.07	-1.50 ± 0.12	-0.671	1.46 ± 0.11	<0.49	0.16
19542+1110	69	0.35 ± 0.05	-1.40 ± 0.16	-0.57 ± 0.04	1.47 ± 0.09	<0.72	0.32 ± 0.04
20087–0308	61	0.46 ± 0.08	-1.45 ± 0.09	-0.42 ± 0.08	0.82 ± 0.06	<0.37	2.79 ± 1.24
20100–4156	80	0.48 ± 0.09	-1.49 ± 0.22	-0.671	0.56 ± 0.05	<0.52	0.15
20414–1651	66	0.54 ± 0.08	-1.68 ± 0.21	-0.70 ± 0.06	1.32 ± 0.12	<0.38	0.15 ± 0.04
F22491–1808	75	0.33 ± 0.04	-1.66 ± 0.26	-0.39 ± 0.08	0.65 ± 0.04	<0.43	0.18 ± 0.05
Mean	70 ± 9	0.43 ± 0.13	-1.30 ± 0.08	...	1.21 ± 0.83	<0.77	0.34 ± 0.55
Median	67 ± 7	0.38 ± 0.12	-1.45 ± 0.07	...	1.14 ± 0.62	<0.65	0.20 ± 0.08

Notes. ^(a) The typical dust temperature uncertainty is ± 3 K. ^(b) Dust optical depth at $350 \mu\text{m}$. For objects with less than four IR photometric points, we assumed a fixed $\tau_{350\mu\text{m}}$ of 0.4 based on the average $\tau_{350\mu\text{m}}$ of the sample. ^(c) We assumed a spectral index of -0.671 for the objects with only one radio observation (see Sect. 4.3). ^(d) Ratio between the flux densities predicted by the gray-body, upper limit free-free, and non-thermal synchrotron models and the observed ~ 220 GHz ALMA continuum flux densities, respectively.

ing objects, we estimated a median non-thermal contribution, which includes both SNe and AGN emission, of 20% and up to 40–60% in four objects: one of the starbursts (09022–3615), one LINER (11095–0238), and 2 out of the 7 systems classified as AGN in the optical (13120–5453, and 16155+0146). The latter suggests that the optical detection of an AGN does not imply that the ~ 220 GHz emission is always dominated by synchrotron AGN emission in local ULIRGs. However, how the AGN synchrotron emission affects the ALMA source sizes is unclear. AGN jets producing synchrotron emission have sizes ranging from pc to few kpc in radio-quiet AGN (Hardcastle & Croston 2020). For instance, the synchrotron radio jet emission from the AGN ULIRG 01572+0009 (PG 0157+001) has a ~ 7 kpc diameter (Leipski et al. 2006), although according to our SED modeling, the synchrotron contribution at 220 GHz is small, about 0.15, and should not affect the estimated size in this object.

For the 5 systems with a high non-thermal contribution, we find that their sizes and luminosity and molecular gas surface densities do not differ from those of the rest of the sample (see Fig. 2).

5.1.3. Summary

It seems likely that these ~ 220 GHz continuum ALMA observations trace the IR emitting region for the majority of local ULIRGs and that the filtered out flux due to the interferometric observations is small. The good agreement between the IR gray-body extrapolation and the ALMA fluxes supports this. Free-free and SNe synchrotron emissions could contribute to the ALMA

flux, but since they have a star-formation origin they should not affect the size estimates for a starburst ULIRG. Synchrotron emission from AGN could bias the size measurements, although we do not find significant differences in size between the 5 systems with high synchrotron emission and the rest of the sample. Therefore, in the following sections we assume that the size of the ~ 220 GHz continuum is equivalent to the size of the region which emits the bulk of the IR luminosity in these ULIRGs.

5.2. Extreme nuclear IR luminosity densities

Using the half-light radius, r_{cont} , of the ALMA continuum and half of the IR luminosity (Sects. 4.1 and 4.3), we calculated the luminosity surface density, $\Sigma_{L_{\text{IR}}}$, in the nuclear regions of the ULIRGs. For systems with 2 nuclei, we estimated their IR luminosity fraction using their relative ALMA continuum fluxes. In 70% of the interacting systems, the luminosity is completely dominated ($>90\%$ of the total luminosity) by one of the nuclei. These fractions and the resulting surface densities are listed in Table 7. We find $\log \Sigma_{L_{\text{IR}}}/(L_{\odot} \text{ kpc}^{-2})$ between 11.5 and 14.3 with a median value of 13.2. If this IR luminosity is produced by SF, it corresponds to $\Sigma_{\text{SFR}} = 2500 M_{\odot} \text{ yr}^{-1} \text{ kpc}^{-2}$ using the Kennicutt & Evans (2012) SFR calibration. These values are much higher (1–2 orders of magnitude) than the densities found in local starburst LIRGs, even when they are observed at higher angular resolutions of ~ 100 pc (e.g., Xu et al. 2015; Pereira-Santaella et al. 2016; Michiyama et al. 2020). Similarly, $z \sim 3$ –6 sub-mm galaxies have lower surface densities, 150 – $1300 M_{\odot} \text{ yr}^{-1} \text{ kpc}^{-2}$ when observed at \sim kpc resolutions (e.g., Riechers et al. 2017; Gómez-

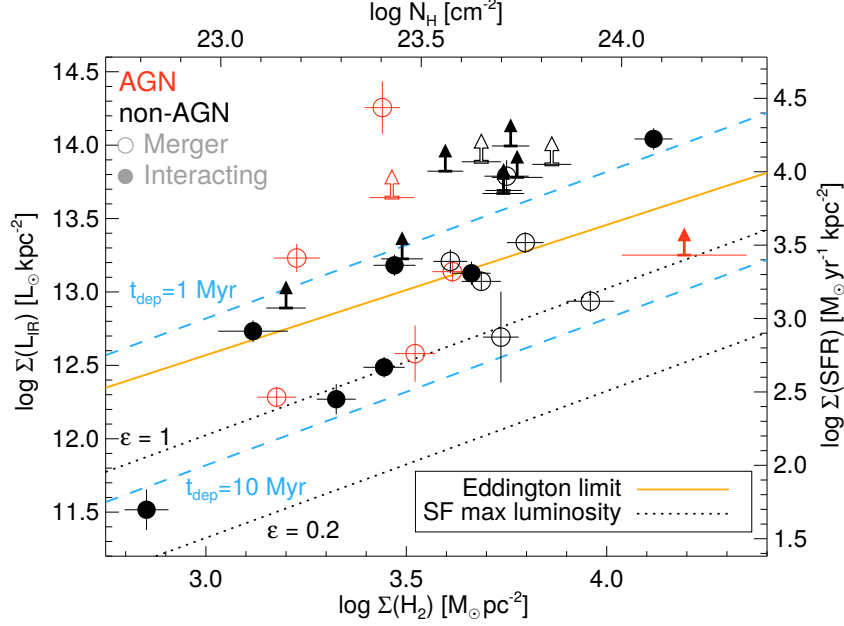


Fig. 7: Cold molecular gas surface density (Σ_{H_2}) vs. IR luminosity surface density (Σ_{LIR}). Galaxy symbols are as in Fig. 5. The dotted black lines indicate the maximum luminosity from an instantaneous starburst using 100% ($\epsilon = 1$) or 20% ($\epsilon = 0.2$) of the available cold molecular gas (see Sect. 5.2.1). The orange solid line is the Eddington luminosity limit. For points above this line, the radiation pressure is stronger than gravity (Sect. 5.5). The dashed blue lines indicate the 1 and 10 Myr depletion times for reference assuming that the IR luminosity is produced by SF. The column density (N_{H}) axis is calculated from Σ_{H_2} assuming a uniform mass distribution (i.e., $N_{\text{H}} = 2 \times \Sigma_{\text{H}_2} / m(\text{H}_2)$ where $m(\text{H}_2)$ is the H_2 molecular weight).

Guijarro et al. 2018). At higher resolutions, ~ 200 pc, these sub-mm galaxies have Σ_{SFR} between 100 and $3000 M_{\odot} \text{ yr}^{-1} \text{ kpc}^{-2}$ which are still lower than the majority of the local ULIRGs (e.g., Oteo et al. 2017; Gullberg et al. 2018).

The observed Σ_{LIR} range is comparable to that measured in local ULIRGs using radio and IR observations at similar angular resolution. Using 33 GHz radio data, Barcos-Muñoz et al. (2017) found a median surface density of $10^{12.8} L_{\odot} \text{ kpc}^{-2}$ in a sample of 22 local interacting/merging systems with $\log L_{\text{IR}} / L_{\odot} > 11.6$. Similarly, González-Alfonso et al. (2015) estimated nuclear $\Sigma_{\text{LIR}} > 10^{12.8} L_{\odot} \text{ kpc}^{-2}$ for 10 local ULIRGs based on the modeling of the far-IR OH absorptions. In addition, mid-IR ground-based studies of ULIRGs derive maximum luminosity densities between $10^{12.1}$ and $10^{14.6} L_{\odot} \text{ kpc}^{-2}$ (Soifer et al. 2000; Imanishi et al. 2011). For the western nucleus of F15327+2340 (Arp 220 W), using higher resolution data (< 50 pc) a luminosity density about $10^{14.3-15.5} L_{\odot} \text{ kpc}^{-2}$ has been estimated (Downes & Eckart 2007; Wilson et al. 2014; Sakamoto et al. 2017). Therefore, our results are compatible with previous findings and confirm that the luminosity density in the nucleus of local ULIRGs is much higher than in other local and high- z starbursts when measured at 100–1000 pc scales.

To investigate the origin of this high Σ_{LIR} values, we discuss two alternatives: an optically thick starburst and the presence of an obscured AGN.

5.2.1. Optically thick starburst

In Fig. 7, we plot the Σ_{LIR} vs. Σ_{H_2} (Sect. 4.2) relation for our sample of local ULIRGs. Based on theoretical models, a Σ_{LIR} of $\sim 10^{13} L_{\odot} \text{ kpc}^{-2}$ has been suggested as the maximum Σ_{LIR} of warm ($T < 200$ K) optically thick starbursts (Thompson et al.

2005). The maximum Σ_{LIR} for these warm starbursts is similar to the median value found in our sample. Hot ($T > 200$ K) optically thick starbursts could have $\Sigma_{\text{LIR}} \sim 10^{15} L_{\odot} \text{ kpc}^{-2}$ when $\Sigma_{\text{H}_2} > 10^6 M_{\odot} \text{ pc}^{-2}$ (Andrews & Thompson 2011). However, we measure $\Sigma_{\text{H}_2} \ll 10^6 M_{\odot} \text{ pc}^{-2}$, so these local ULIRGs might be more similar to the warm optically thick starburst models.

Although the Σ_{LIR} are similar to the maximum for a warm optically thick starburst, when combined with the Σ_{H_2} , the resulting depletion times, $\Sigma_{\text{H}_2} / \Sigma_{\text{SFR}}$, would be shorter (< 1 – 15 Myr; see Table 7) than those measured in other LIRG starbursts (> 30 – 100 Myr; Xu et al. 2015; Pereira-Santaella et al. 2016).

We also estimated the maximum Σ_{LIR} that a starburst can produce for a given Σ_{H_2} . Using STARBURST99 (Leitherer et al. 1999), we find that the maximum luminosity produced by a solar metallicity instantaneous burst, assuming a Kroupa (2001) initial mass function (IMF), is $\sim 1060 L_{\odot} M_{\odot}^{-1}$ at an age of ~ 2.2 Myr (see also Sakamoto et al. 2013). In Fig. 7, we show this limit ($\epsilon = 1$ dotted black line). This limit assumes that all the molecular gas is instantaneously transformed into stars (i.e., 100% efficient SF). In reality, stellar feedback dissipates the molecular clouds before a 100% efficiency is achieved, so the maximum luminosity from a starburst would be lower than this limit. Based on magnetohydrodynamic simulations, the maximum efficiency per free-fall time is about 20% (e.g., Padoan et al. 2012) which is shown in Fig. 7 too ($\epsilon = 0.2$). This figure shows that 70% of the nuclei are above the 100% efficiency limit ($\epsilon = 1$) and all of them are above this 20% efficiency limit.

In addition, if the nuclear luminosity is produced by a compact and intense starburst, a continuous supply of molecular gas to the nucleus would be required to sustain the ongoing SFR level. Otherwise, it would not be possible to achieve the observed Σ_{LIR} which implies depletion times < 1 Myr in 30% of the sample and < 15 Myr in all of them. However, the high radiation pres-

Table 7: Nuclear properties

IRAS name	Nucleus	Frac. ^a	$\log \Sigma_{L_{\text{IR}}}^b$ ($L_{\odot} \text{ kpc}^{-2}$)	t_{dep}^c (Myr)	Above Eddington limit? ^d	Optical AGN? ^e	CON ^f	HCN $14\mu\text{m}^g$
00091–0738	S	0.97	>13.67	<0.78	Y	N	...	Y
	N	<0.03	
00188–0856	-	1.00	13.15±0.08	2.0±0.1	Y	Y	...	N
00509+1225	-	1.00	13.30±0.09	0.65±0.09	Y	Y	...	N
01572+0009	-	1.00	14.30±0.18	0.10±0.01	Y	Y	...	N
F05189–2524	-	1.00	>13.70	<0.4	Y	Y	...	Y
07251–0248	W	0.09	12.74±0.07	1.6±0.3	Y	N	...	Y
	E	0.91	>13.78	<0.65	Y	N	...	
09022–3615	-	1.00	12.70±0.24	7.3±0.7	N	N	N	N
F10190+1322	W	0.12	11.53±0.11	14.3±1.8	N	N	...	N
	E	0.88	12.50±0.08	6.0±0.7	N	N	...	
11095–0238	SW	0.32	>12.88	<1.3	Y	N	...	Y
	NE	0.68	>13.22	<1.2	Y	N	...	
F12112+0305	SW	0.09	12.27±0.12	7.5±0.8	N	N	...	N
	NE	0.91	>14.00	<0.38	Y	N	?	
13120–5453	-	1.00	12.59±0.23	5.8±0.7	N	Y	N	N
F14348–1447	SW	0.63	>13.83	<0.39	Y	N	N	N
	NE	0.37	13.19±0.08	1.3±0.2	Y	N	N	
F14378–3651	-	1.00	12.29±0.07	5.2±0.6	N	Y	?	N
F15327+2340	W	0.71	>13.89	0.42±0.05	Y	N	Y	Y
	E	0.29	13.07±0.07	2.7±0.3	N	N	?	
16090–0139	-	1.00	12.94±0.07	7.0±0.9	N	N	...	Y
16155+0146	NW	0.80	>13.26	<5.8	?	Y	...	N
	SE	< 0.2	
17208–0014	-	1.00	>13.88	<0.65	Y	N	Y	Y
F19297–0406	S	< 0.01	Y
	N	0.99	13.13±0.07	2.3±0.2	N	N	...	
19542+1110	-	1.00	13.22±0.07	1.7±0.2	Y	N	...	N
20087–0308	-	1.00	13.32±0.06	2.0±0.2	Y	N	...	N
20100–4156	NW	<0.02	Y
	SE	0.98	14.04±0.07	0.78±0.09	Y	N	...	
20414–1651	-	1.00	13.80±0.11	0.60±0.08	Y	N	...	N
F22491–1808	W	<0.02	Y
	E	0.98	>13.69	<0.74	Y	N	Y	

Notes. ^(a) Fraction of the total IR luminosity (Table 1) which is assigned to each nucleus based on their relative ALMA continuum fluxes. ^(b) Logarithm of the IR luminosity surface density assuming the source size of the ALMA continuum (Table 3). ^(c) Depletion time using the molecular gas surface density from Table 4 and the IR luminosity surface density in this Table assuming that the latter is completely produced by SF. ^(d) Indicates if the nucleus is above (Y), or not (N), the Eddington limit estimated in Sect. 5.5. ^(e) Indicates whether an AGN is detected (Y), or not (N), from optical spectroscopy. See also Table 1. ^(f) Objects classified as CONs based on their HCN-vib luminosity (see Falstad et al. 2021). “?” indicates that HCN-vib emission is detected but below the CON threshold ($\Sigma_{\text{HCN-vib}} < 1 L_{\odot} \text{ pc}^{-2}$). ^(g) Indicates if the mid-IR HCN-vib $14\mu\text{m}$ absorption is detected in the system integrated *Spitzer*/IRS spectra from the archive (see also Lahuis et al. 2007).

sure in the nucleus, which is compatible with being above the Eddington limit for 67% of the nuclei (see Sect. 5.5), could prevent these massive gas inflows.

5.2.2. Or obscured AGN?

We find that 70% of the ULIRGs have $\Sigma_{L_{\text{IR}}}/\Sigma_{\text{H}_2}$ ratios above the limit for a $\epsilon = 1$ efficient starburst. Also, 65% have $\Sigma_{L_{\text{IR}}}$ above the theoretical value of an optically thick warm starburst ($\sim 10^{13} L_{\odot} \text{ kpc}^{-2}$). These fractions are similar for systems optically classified as AGN and starbursts (see Fig. 7). These results suggest that what produces the bulk of the IR luminosity in these local ULIRGs is not a standard starburst.

Alternatively, an AGN could dominate the L_{IR} of these objects. This possibility has also been suggested because of the

high $\Sigma_{L_{\text{IR}}}$ in the ULIRG nuclei derived from mid-IR data (e.g., Imanishi et al. 2011) or from the mm continuum in Arp 220 (e.g., Downes & Eckart 2007; Wilson et al. 2014; Scoville et al. 2017; Sakamoto et al. 2017). From Σ_{H_2} , we estimate that the nuclear H column densities are moderate, between 10^{23} and 10^{24} cm^{-2} (see Fig. 7). These values are lower than the Compton thick limit ($\sim 2 \times 10^{24} \text{ cm}^{-2}$), so we would expect the AGN X-ray emission not to be completely absorbed. Iwasawa et al. (2011) observed a sample of local U/LIRGs with *Chandra* at 0.5–7 keV. Twelve out of our 25 systems are part of their sample. They found AGN evidence in 6 out of the 12, but they estimated low AGN contributions to the L_{IR} (3–20%). However, it is possible that the actual N_{H} that obscures these AGN is actually higher and could absorb the 0.5–7 keV X-ray emission. Our N_{H} estimates are based on molecular gas observations at $\sim 400 \text{ pc}$ resolution, but the obscuring molecular torus could be smaller, as observed in local

Seyfert galaxies (median diameter of 40 pc; [Garcia-Burillo et al. 2021](#)), so our N_{H} values might be underestimated.

To minimize the effects of the obscuring column density, we also considered the *Swift*-BAT 105-Month 14–195 keV survey ([Oh et al. 2018](#)). This higher energy X-ray band is less affected by N_{H} than the *Chandra* 0.5–7 keV range. The 5σ sensitivity of the survey is $8.4 \times 10^{-12} \text{ erg s}^{-1} \text{ cm}^{-2}$. Only one source in our sample, F05189–2524, is detected at 14–195 keV. For the rest of the targets, the *Swift*-BAT survey implies $L_{14-195 \text{ keV}} < 10^{43.3-44.8} \text{ erg s}^{-1}$, depending on the distance. Assuming that the bolometric AGN luminosity is $L_{\text{AGN}} \sim 12 \times L_{14-195 \text{ keV}}$ ([Marconi et al. 2004](#)), the 5σ upper limits would correspond to $L_{\text{AGN}} < 10^{44.3-45.9} \text{ erg s}^{-1} = 10^{10.7-12.3} L_{\odot}$. This would result in an AGN contribution $L_{\text{AGN}}/L_{\text{IR}} < 0.45$ for all but one of these ULIRGs and a median upper limit of < 0.25 . More sensitive NuSTAR $> 10 \text{ keV}$ observations were presented by [Teng et al. \(2015\)](#). Their sample contains four of our ULIRGs, three of them already classified as Sy in the optical. One is undetected (F14378–3651), in F15327+2340 (Arp 220) no AGN evidence is found, although a very deeply buried AGN is still possible, and F05189–2524 and 13120–5453 are Compton-thin and -thick AGN, respectively.

ULIRGs are known to be hard X-ray underluminous ([Imanishi & Terashima 2004; Teng et al. 2015](#)) and AGN in mergers are also heavily obscured ([Ricci et al. 2017](#)). The combination of these two factors could explain why the AGN in these sources, if present, remain mostly undetected in X-ray observations.

As discussed before, the high $\Sigma_{\text{LIR}}/\Sigma_{\text{H}_2}$ nuclear ratios cannot be easily explained by a starburst, even if an optically thick one is considered. These ALMA data would be consistent with an AGN dominating the IR luminosity, but it is not possible to confirm that an AGN is present in the nuclei of the majority of these ULIRGs. The non-detection of these possible AGN in ultra-hard X-ray observations could indicate extremely high obscuring column densities. Higher angular resolution ALMA data could spatially resolve the obscuring material and establish its actual column density as in nearby Seyfert galaxies (e.g., [Garcia-Burillo et al. 2021](#)).

5.2.3. Systematic uncertainties

There are several assumptions which could bias the Σ_{LIR} and Σ_{H_2} values presented in Fig. 7. For instance, the r_{CO} size used to estimate the nuclear Σ_{H_2} is larger than the r_{cont} used for Σ_{LIR} . This is because the CO(2–1) emission is more extended than the $\sim 220 \text{ GHz}$ continuum ($r_{\text{CO}}/r_{\text{cont}} = 2.5 \pm 1.1$; see Sect. 4.2) and it is not possible to exactly determine the amount of CO(2–1) within the r_{cont} region since, in most cases, both r_{cont} and r_{CO} are smaller than the beam size. Therefore, Σ_{H_2} are averaged over larger regions than Σ_{LIR} and the true nuclear Σ_{H_2} could be higher. Consequently, the real star-formation efficiency (depletion time) could be lower (longer). Actually, [González-Alfonso et al. \(2015\)](#), by modeling the far-IR OH absorptions, estimated nuclear Σ_{H_2} between $10^{3.8}$ and $10^{4.7} M_{\odot} \text{ pc}^{-2}$ for 10 local ULIRGs. These values are ~ 5 times higher than our average Σ_{H_2} derived from CO(2–1) using $\sim 400 \text{ pc}$ resolution data. In addition, 8 of our targets are part of a survey to detect vibrationally excited HCN emission to identify compact obscured nuclei (CONs). The HCN-vib (3–2) 267.199 GHz line is detected in 5 of these systems ($63 \pm 18\%$; see Table 7 and [Imanishi et al. 2016, 2019; Falstad et al. 2021](#)). Similarly, the mid-IR HCN-vib $14 \mu\text{m}$ absorption, which populates the levels originating the HCN-vib emission, is detected in 10 (6 interacting systems and 4 mergers) out of the 23 systems ($43 \pm 10\%$ globally, $60 \pm 15\%$

of the interacting systems and $31 \pm 13\%$ of the advanced mergers; Table 7). The presence of these HCN-vib spectral features suggests the presence of extreme nuclear column densities too. Higher resolution CO(2–1) data will help us to establish the cold molecular gas density more accurately. The already available high resolution CO(2–1) data for 17208–0014 (120 pc resolution; see Sect. 4.1.1), suggest a factor of 2 higher nuclear Σ_{H_2} ([Pereira-Santaella in prep.](#)). However, for this galaxy, the nuclear Σ_{LIR} also increases by a factor of ~ 5 using these data, so the resulting $\Sigma_{\text{SFR}}/\Sigma_{\text{H}_2}$ ratio would be even higher and reinforce the need for an obscured AGN in this object.

Another uncertainty related to the Σ_{H_2} is the α_{CO} conversion factor. We assumed a ULIRG-like factor, which is relatively low compared to the conversion factor used for normal galaxies (see e.g., [Bolatto et al. 2013](#)). High nuclear column densities can produce self-absorbed CO(2–1) line profiles as seen in the compact nuclei of some local LIRGs (e.g., [Sakamoto et al. 2013; Pereira-Santaella et al. 2017; González-Alfonso et al. 2021](#)). If the nuclear CO(2–1) emission of these ULIRGs is self-absorbed, the assumed ULIRG-like α_{CO} conversion factor could result in underestimated Σ_{H_2} values. For this paper, we opt to use the standard ULIRG-like α_{CO} , as it is typically done in local ULIRG studies, but we will investigate the presence of self-absorbed CO(2–1) profiles in these targets in a future paper. The depletion times depend on the assumed α_{CO} conversion factor. If the actual α_{CO} of these objects is similar to the Milky Way factor (i.e., 5 times higher; [Bolatto et al. 2013](#)), the molecular gas mass will be 5 times higher, and the depletion times 5 times longer. However, the median t_{dep} would still be very short ($< 6 \text{ Myr}$).

Finally, the maximum luminosity for a starburst (dotted lines in Fig. 7) is calculated using a [Kroupa \(2001\)](#) IMF. If the IMF in ULIRGs is top-heavy as suggested by some works (see e.g., [Sliwa et al. 2017; Brown & Wilson 2019](#)), the maximum starburst luminosity per unit of molecular gas could be higher. For example, the maximum luminosity for an IMF truncated at $30 M_{\odot}$ would produce ~ 10 times more luminosity per unit of molecular gas than the standard [Kroupa \(2001\)](#) IMF. For an $\epsilon = 0.2$ efficiency, this top-heavy IMF could explain the $\Sigma_{\text{LIR}}/\Sigma_{\text{H}_2}$ ratios observed in about half of the nuclei, although these starbursts would have radiation pressures above the Eddington limit and they would not be stable on short timescales of few Myr (see Sect. 5.5).

5.3. Continuum and CO(2–1) sizes vs. mid-infrared excess

In the left panel of Fig. 8, we show the relation between the excess mid-IR emission (Sect. 4.3.1) and the 220 GHz continuum size, r_{cont} . We note that the excess mid-IR emission is estimated from the system integrated *Spitzer*/IRS spectra. Therefore, in interacting systems where a nuclei dominates the total L_{IR} , the mid-IR excess of the secondary nucleus cannot be directly estimated from this integrated spectrum. Thus, we excluded the 8 nuclei in interacting systems with IR luminosity fractions $< 20\%$ (see Table 7). In this diagram, we can classify the ULIRG nuclei in two main groups: compact objects ($r_{\text{cont}} < 120 \text{ pc}$) with high mid-IR excess (logarithm > -0.9 ; red box); and objects following a linear relationship between the two properties with decreasing excess mid-IR emission for decreasing r_{cont} (blue line).

The first group exclusively contains objects classified as AGN in the optical. We note that the 2 interacting systems in our sample with no ALMA data, F12072–0444 and F13451+1232, are optical AGN with $\log \Delta L_{6-20 \mu\text{m}}/L_{\text{IR}} > -0.9$ and could lie in this region of the diagram as well. The location of these AGN in this diagram (red box) is what is expected if warm dust (which

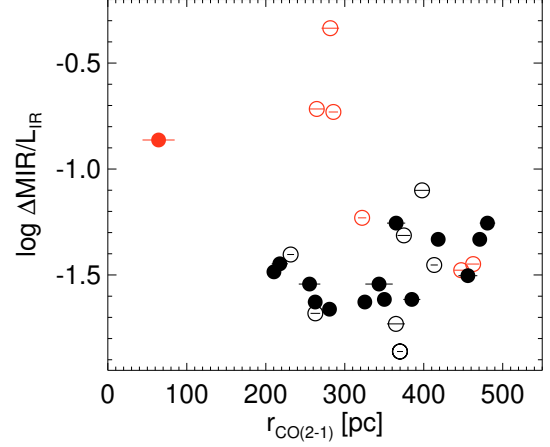
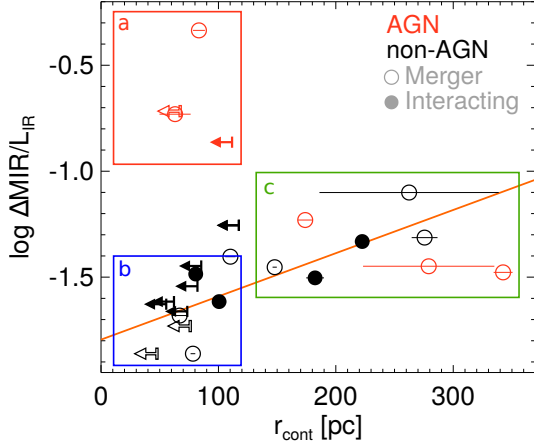


Fig. 8: Logarithm of the excess mid-IR emission vs. size of the 220 GHz continuum (left panel) and size of the CO(2–1) emission (right panel). Galaxy symbols are as in Fig. 5. The solid orange line is the best linear fit to the non-AGN (black) points. In the left panel, the red box (a) marks a region of this diagram solely occupied by optically detected AGN. The blue box (b) indicates the location of very compact ULIRG nuclei (mostly unresolved by our data) with negligible excess mid-IR emission. The green box shows the location of more extended nuclei with higher mid-IR excess.

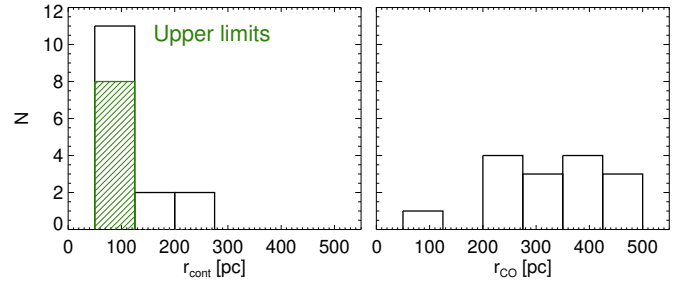
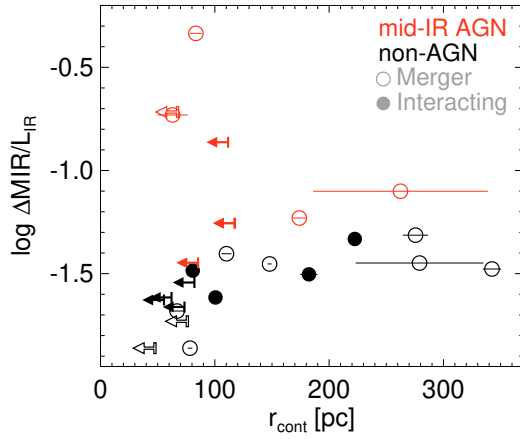


Fig. 10: Distribution of the 220 GHz continuum radius r_{cont} (left) and the CO(2–1) emission radius r_{CO} (right) for the nuclei in interacting ULIRGs. The upper limits for the 220 GHz continuum are included in the first bin and indicated by the green shaded area.

Fig. 9: Same as left panel of Fig. 8, but galaxies with more than 50% AGN contribution based on mid-IR observations are indicated in red (Veilleux et al. 2009; Nardini et al. 2010).

emits in the mid-IR) from a compact torus produces a significant part of their total L_{IR} . Actually, the mid-IR $f_{15\mu\text{m}}/f_{30\mu\text{m}}$ color, which behaves similar to the mid-IR excess, have been used to estimate the AGN luminosity contribution in ULIRGs (e.g., Veilleux et al. 2009).

For the remaining nuclei there is a correlation ($r_s = 0.87$ and $p = 1 \times 10^{-3}$) between the continuum size and the mid-IR excess with increasing sizes for increasing mid-IR excess emission. The size of these sources ranges from <70 pc to ~ 300 pc and the best linear fit is $\log \Delta L_{6-20\mu\text{m}}/L_{\text{IR}} = (-1.8 \pm 0.1) + (2.2 \pm 0.6) \times 10^{-3} \times r_{\text{cont}}/\text{pc}$.

In Fig. 8 (left panel), we highlighted (blue box) sources with $r_{\text{cont}} < 120$ pc. This box contains 46% of the sample (12 nuclei out of 26). They have sizes comparable to the AGN (red box), although most of them only have an upper limit r_{cont} , so their real size could be lower than that of the AGN. Opposite to most AGN, which have excess mid-IR emission between 15 and 70% of the L_{IR} , these objects have negligible mid-IR excess

($<3\%$). A majority of the nuclei in interacting systems (60%) lie in this blue box while it only includes 30% of the mergers. Actually, mergers following this relation have larger radii (median 160 pc) than the interacting systems (median 90 pc). This suggests that during the early phases of the interaction (nuclear separation > 1 kpc), most of the activity (AGN and/or SF) occurs in compact regions where most of the mid-IR emission is absorbed by dust and then re-emitted in the far-IR. Then, in more advanced merger stages (nuclear separation < 1 kpc), the activity appears on more extended regions (green box in Fig. 8), unless an optically detected AGN is present (red box sources).

In Fig. 9, we indicate the systems with AGN contributions $>50\%$ based on mid-IR observations (Veilleux et al. 2009; Nardini et al. 2010). The majority of the optical AGN are also classified as AGN by these mid-IR diagnostics (5 out of 7) and only 3 non-Sy are identified as mid-IR AGN. In addition, this figure shows that there is a good correlation between the mid-IR AGN classification and the mid-IR excess. This is because these mid-IR diagnostics are based on the detection of warm dust which is closely related to the mid-IR excess definition used here. Therefore, if the mid-IR emission of the AGN in these ULIRGs is

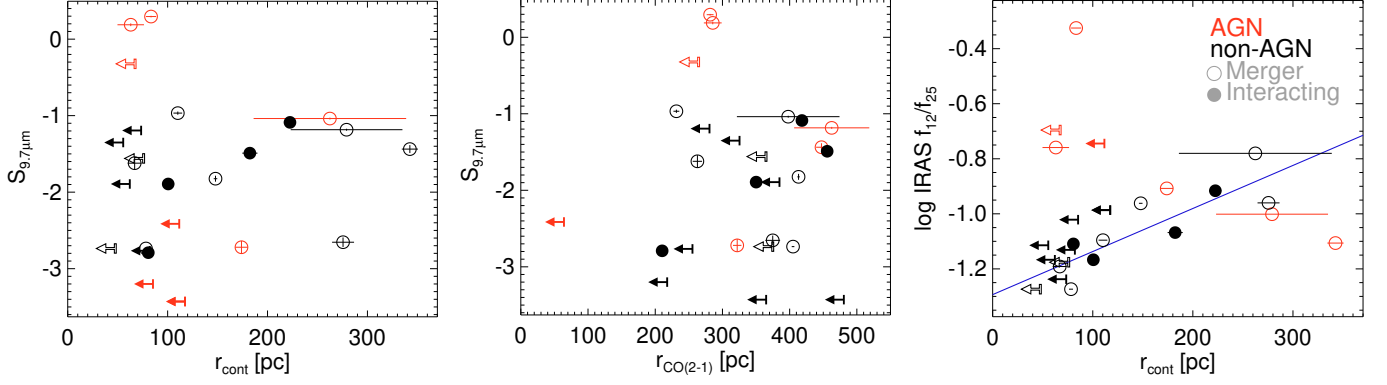


Fig. 11: Relation between the 9.7 μm silicate absorption and the 220 GHz continuum (left) and the CO(2-1) (middle) sizes. The right panel shows the 220 GHz continuum size vs. IRAS 12 μm /25 μm color relation. Symbols as in Fig. 5. For the IRAS 12 μm /25 μm color relation (right), the best linear fit to the non-AGN objects (black symbols) is $\log f_{12}/f_{25} = (-1.29 \pm 0.04) + (1.6 \pm 0.3) \times 10^{-3} \times r_{\text{cont}}/\text{pc}$.

absorbed (see also Sect. 5.4), these mid-IR diagnostics could fail to detect them.

The right panel of Fig. 8 shows the excess mid-IR emission as function of the molecular gas emission size r_{CO} . We do not find a significant correlation between the molecular gas size and the mid-IR excess ($r_s = 0.34$ and $p = 0.12$). The molecular gas emission size is similar in the interacting systems and advanced mergers (median ~ 350 pc). On the contrary, hydrodynamic simulations predict that strong torques during the first passage can pile up the gas in $\sim \text{kpc}$ -scale starbursts and later, during the final-coalescence, in more compact sub-kpc starbursts (e.g., Hopkins et al. 2013).

We find that, for the interacting systems, the molecular gas and the continuum size distributions are very different (see Fig. 10). The radii of the molecular gas emission is uniformly distributed over the whole observed range (mostly between 200 and 500 pc; right panel of Fig. 10) while the continuum size distribution peaks at compact radii (< 100 pc; left panel of Fig. 10). This suggests that, even if there is a global correlation between the continuum and the CO emission sizes for the whole sample of ULIRGs (see Sect. 4.2 and Fig. 2), for the interacting systems, the two sizes seem to be decoupled. An obscured AGN, which do not need large amounts of molecular gas to produce high luminosities, could explain why these interacting nuclei have very compact continuum sources but a more extended molecular gas distribution.

5.4. Continuum size vs. silicate absorption and IR colors

In this section, we explore possible relations between the 220 GHz continuum size and other IR tracers. As in Sect. 5.3, we excluded from this analysis nuclei with contributions $< 20\%$ to the total IR luminosity of the systems. We first consider the 9.7 μm silicate absorption. We use the 9.7 μm silicate strengths from the Infrared Database of Extragalactic Observables from Spitzer (IDEOS; Table A.1; Hernán-Caballero et al. 2020, Spoon et al. in prep.). Deep silicate absorptions have been associated with an evolutionary phase in which the obscuring molecular cocoon created during the early interaction phases have not been yet shed (e.g., Spoon et al. 2007). Therefore, we could expect a relation between the silicate absorption and the size of the cold molecular or dust continuum emissions. However, we find no significant correlation between them (see left and middle pan-

els of Fig. 11). To explain this absence of correlation, we argue that to measure deep 9.7 μm silicate absorptions, some mid-IR radiation must escape the nuclear molecular cocoon. As shown in Sect. 5.3, the fraction of the total IR emission that is emitted in the mid-IR is greatly reduced in the most compact nuclei (i.e., the mid-IR emission is absorbed and then re-emitted in the far-IR). Therefore, the 9.7 μm silicate absorption is not necessarily extreme in these compact sources since their nuclear mid-IR emission is possibly absorbed and what is observed in the mid-IR is likely produced by less obscured external regions. The presence of several CONs in our sample (see Falstad et al. 2021), is also consistent with the mid-IR emission of the hot nucleus being obscured. Likewise, ground-based mid-IR spectroscopy of local AGN ULIRGs showed that their silicate absorptions are produced by dust not directly associated with the AGN (Alonso-Herrero et al. 2016). This scenario is also supported by radiative transfer models of compact nuclei where the mid-IR emission is completely absorbed for objects with very high column densities ($N_{\text{H}_2} > 10^{25} \text{ cm}^{-2}$; see fig. 2 of González-Alfonso & Sakamoto 2019).

We also studied possible correlations between the broadband IRAS colors and the size of the continuum and cold molecular emissions. Most of the ULIRGs are undetected by IRAS at 12 μm , for this reason we computed synthetic fluxes for the four IRAS bands (12, 25, 60, and 100 μm) from the *Spitzer*/IRS spectrum and the IR SED model (Sect. 4.3). We tried the 6 IRAS color combinations. Only the f_{12}/f_{25} color shows a significant correlation with the continuum size (Fig. 11 right). The f_{12}/f_{25} ratio is actually related to the mid-IR emission. The 12 μm flux would trace the mid-IR emission while at 25 μm , the emission is dominated by the IR gray-body for most of the non-AGN ULIRGs. Therefore, this relation would be equivalent to that presented in Sect. 5.3 with the mid-IR excess emission.

5.5. Nuclear radiation pressure. Eddington limit

We find very high Σ_{LIR} in the nuclei of the ULIRGs, so it is important to determine if the radiation pressure can overcome the gravity attraction in these objects. To do so, we calculated the Eddington limit in the Σ_{H_2} - Σ_{LIR} plane by fitting the model results reported by González-Alfonso & Sakamoto (2019). These models assume spherical symmetry and accurately determine the force due to radiation pressure once the equilibrium T_{dust} profile

across the source is calculated. The models assume a density profile $\sim r^{-1}$, such that Σ_{H_2} does not depend on the source radius. Our fitting, shown in Fig. 7 with an orange line, is approximately valid for $\Sigma_{\text{H}_2} \lesssim 3 \times 10^4 \text{ M}_\odot \text{ pc}^{-2}$, and assumes an intermediate molecular gas fraction with respect to the total mass, $f_g = 0.3$, and a gas-to-dust ratio of $f_{\text{gd}} = 100$ by mass. In the optically thick limit, the Eddington luminosity is proportional to $f_g^{-1/2} \times f_{\text{gd}}$ (Andrews & Thompson 2011).

Fig. 7 shows that half of the nuclei, 19 out of the 29, are above the estimated Eddington limit (see also Table 7). This suggests that the radiation pressure can be stronger than gravity in these nuclei and, therefore, massive gas outflows are expected. This result is consistent with the detection of massive molecular outflows in local ULIRGs (Sturm et al. 2011; Ciccone et al. 2014; González-Alfonso et al. 2017; Pereira-Santaella et al. 2018; Lutz et al. 2020) and also supports that radiation pressure plays a relevant role as a potential launching mechanism of the outflows in local ULIRGs.

6. Conclusions

We have analyzed new high-resolution ALMA ~ 220 GHz and CO(2–1) observations of a representative sample of 23 local ULIRGs (34 individual nuclei) as part of the Physics of ULIRGs with MUSE and ALMA (PUMA) project (see also Perna et al. 2021). The main results of this work are the following:

1. We modeled the ~ 220 GHz (190–250 GHz) continuum emission of these ULIRGs. We find that the median deconvolved half light radius (r_{cont}) is 80–100 pc and about 40% (11/29 with continuum detection) of the nuclei are not resolved by these data. From the IR and radio SED modeling, we obtain that the ALMA ~ 220 GHz continuum fluxes are in good agreement, within a factor of 2 (median ratio of 1.1 ± 0.7), with the extrapolation of the dust far-IR gray body emission. This suggests that the ~ 220 GHz continuum traces the regions emitting the bulk of the IR luminosity in these objects. We estimate that the contributions from synchrotron ($\sim 20\%$) and free-free emission ($< 65\%$) to the ALMA flux are not likely to bias the measured sizes. Using the ~ 220 GHz continuum size, we calculate IR luminosity densities, Σ_{LIR} , in the range $10^{11.5} - 10^{14.3} L_\odot \text{ kpc}^{-2}$ (median $10^{13.2} L_\odot \text{ kpc}^{-2}$), which is equivalent to $\Sigma_{\text{SFR}} = 2500 \text{ M}_\odot \text{ yr}^{-1} \text{ kpc}^{-2}$. This is similar to the range derived from previous radio and ground-based mid-IR observations and 1–2 orders of magnitude brighter than local and high- z starbursts.
2. Similarly, we measure deconvolved CO(2–1) emission sizes, r_{CO} , between 60 and 700 pc. These are on average 2.5 ± 1.1 times larger than the ~ 220 GHz continuum size. We find no differences between systems optically classified as AGN or starburst or between interacting systems and advanced mergers. Using a ULIRG-like α_{CO} conversion factor, we find nuclear molecular gas surface densities, Σ_{H_2} , in the range $10^{2.9} - 10^{4.2} \text{ M}_\odot \text{ pc}^{-2}$.
3. If the L_{IR} is produced by SF, the $\Sigma_{\text{LIR}}/\Sigma_{\text{H}_2}$ ratios imply extremely short molecular gas depletion times ($< 1\text{--}15$ Myr). In addition, 70% of the nuclei would have SF efficiencies above the maximum for a starburst ($\epsilon = 1$) and all of them would have $\epsilon > 0.2$, which is the maximum efficiency per free-fall time predicted by simulations. These findings suggests that the bulk of the IR luminosity of these ULIRGs does not originate in a nuclear starburst. An obscured AGN with $L_{\text{AGN}}/L_{\text{IR}} > 0.5$ would be an alternative energy source.
4. For the compact nuclei ($r_{\text{cont}} < 120$ pc) in interacting system with low mid-IR excess emission, the r_{cont} is not correlated with the cold molecular gas emission, r_{CO} , which varies between 200 and 500 pc. This could support the presence of a deeply embedded AGN which, opposed to star-formation, would not require large amounts of cold molecular gas to produce the observed high IR luminosities.
5. The presence of compact and extremely embedded nuclei is supported by the detection of the HCN-vib $14 \mu\text{m}$ absorption in $43 \pm 10\%$ of the sample. The detection rate is higher, $60 \pm 15\%$, in interacting systems than in advanced mergers, $31 \pm 13\%$.
6. The ULIRG nuclei can be classified in two groups in the 220 GHz continuum size, r_{cont} , vs. mid-IR excess emission, $\Delta L_{6-20 \mu\text{m}}$, diagram. $\Delta L_{6-20 \mu\text{m}}$ is the 6–20 μm emission excess after subtracting the far-IR gray-body contribution in this wavelength range. These two groups are: (a) compact ($r_{\text{cont}} < 120$ pc) nuclei with high mid-IR excess emission ($\log \Delta L_{6-20 \mu\text{m}}/L_{\text{IR}} > -0.9$) which are optically classified AGN; and (b) objects that follow a relation with decreasing r_{cont} for decreasing mid-IR excess emission. A majority of the nuclei in interacting systems (60%) that follow this relation have $r_{\text{cont}} < 120$ pc, which are at the lower end of the r_{cont} -mid-IR excess relation, while only 30% of the mergers have these compact continuum emission. Mergers following this relation have larger sizes on average. This suggest that in the early stages of the interaction (nuclear separation > 1 kpc) most of the activity occurs in very compact regions while, in more advanced merger stages, the activity is more extended unless and optically detected AGN is present.
7. We find no correlation between the $9.7 \mu\text{m}$ silicate absorption and the ~ 220 GHz continuum or CO(2–1) sizes. The relatively faint mid-IR emission of the most compact nuclei could prevent the presence of deep silicate absorptions in their mid-IR spectra and this could hinder the use of this absorption feature to find some obscured nuclei.
8. We find that 67% (19/29) of the nuclei have nuclear radiation pressures above the estimated Eddington limit. This is consistent with the presence of massive molecular outflows in ULIRGs and supports that radiation pressure can have a relevant role in the outflow launching process.

Acknowledgements. We thank the referee for the useful comments and suggestions. We are grateful to A. Hernán-Caballero and H. Spoon for providing measurements from the IDEOS database. MPS and IL acknowledge support from the Comunidad de Madrid through the Atracción de Talento Investigador Grant 2018-T1/TIC-11035 and PID2019-105423GA-I00 (MCIU/AEI/FEDER,UE). AA-H and SG-B acknowledge support through grant PGC2018-094671-B-I00 (MCIU/AEI/FEDER,UE). MP is supported by the Programa Atracción de Talento de la Comunidad de Madrid via grant 2018-T2/TIC-11715. AL acknowledges the support from Comunidad de Madrid through the Atracción de Talento Investigador Grant 2017-T1/TIC-5213. SA, LC, MP, and AL acknowledge support from the Spanish Ministerio de Economía y Competitividad through grants ESP2017-83197-P and PID2019-106280GB-I00. This work was done under project No. MDM-2017-0737 Unidad de Excelencia "María de Maeztu"- Centro de Astrobiología (INTA-CSIC). D. Rigopoulou acknowledges support from STFC through grant ST/S000488/1. This paper makes use of the following ALMA data: ADS/JAO.ALMA#2015.1.00113.S, ADS/JAO.ALMA#2015.1.00263.S, ADS/JAO.ALMA#2016.1.00170.S, ADS/JAO.ALMA#2016.1.00777.S, ADS/JAO.ALMA#2018.1.00486.S, and ADS/JAO.ALMA#2018.1.00699.S. ALMA is a partnership of ESO (representing its member states), NSF (USA) and NINS (Japan), together with NRC (Canada) and NSC and ASIAA (Taiwan) and KASI (Republic of Korea), in cooperation with the Republic of Chile. The Joint ALMA Observatory is operated by ESO, AUI/NRAO and NAOJ. The National Radio Astronomy Observatory is a facility of the National Science Foundation operated under cooperative agreement by Associated Universities, Inc.

References

- Abel, N. P., Dudley, C., Fischer, J., Satyapal, S., & van Hoof, P. A. M. 2009, *ApJ*, 701, 1147
- Alonso-Herrero, A., Esquej, P., Roche, P. F., et al. 2016, *MNRAS*, 455, 563
- Alonso-Herrero, A., Ramos Almeida, C., Esquej, P., et al. 2014, *MNRAS*, 443, 2766
- Andrews, B. H. & Thompson, T. A. 2011, *ApJ*, 727, 97
- Arribas, S., Colina, L., Alonso-Herrero, A., et al. 2012, *A&A*, 541, A20
- Baan, W. A. & Klöckner, H.-R. 2006, *A&A*, 449, 559
- Barcos-Muñoz, L., Leroy, A. K., Evans, A. S., et al. 2017, *ApJ*, 843, 117
- Barcos-Muñoz, L., Leroy, A. K., Evans, A. S., et al. 2015, *ApJ*, 799, 10
- Barvainis, R. & Antonucci, R. 1989, *ApJS*, 70, 257
- Bolatto, A. D., Wolfire, M., & Leroy, A. K. 2013, *ARA&A*, 51, 207
- Brown, T. & Wilson, C. D. 2019, *ApJ*, 879, 17
- Casey, C. M., Narayanan, D., & Cooray, A. 2014, *Phys. Rep.*, 541, 45
- Chu, J. K., Sanders, D. B., Larson, K. L., et al. 2017, *ApJS*, 229, 25
- Cicone, C., Maiolino, R., Sturm, E., et al. 2014, *A&A*, 562, A21
- Clemens, M. S., Vega, O., Bressan, A., et al. 2008, *A&A*, 477, 95
- Condon, J. J., Cotton, W. D., Greisen, E. W., et al. 1998, *AJ*, 115, 1693
- Condon, J. J., Helou, G., Sanders, D. B., & Soifer, B. T. 1990, *ApJS*, 73, 359
- Condon, J. J., Helou, G., Sanders, D. B., & Soifer, B. T. 1996, *ApJS*, 103, 81
- Condon, J. J., Huang, Z. P., Yin, Q. F., & Thuan, T. X. 1991, *ApJ*, 378, 65
- Condon, J. J. & Ransom, S. M. 2016, *Essential Radio Astronomy*
- Díaz-Santos, T., Charmandaris, V., Armus, L., et al. 2010, *ApJ*, 723, 993
- Downes, D. & Eckart, A. 2007, *A&A*, 468, L57
- Duc, P. A., Mirabel, I. F., & Maza, J. 1997, *A&AS*, 124, 533
- Falstad, N., Aalto, S., König, S., et al. 2021, *arXiv e-prints*, arXiv:2102.13563
- García-Burillo, S., Alonso-Herrero, A., Ramos Almeida, C., et al. 2021, *arXiv e-prints*, arXiv:2104.10227
- Genzel, R., Lutz, D., Sturm, E., et al. 1998, *ApJ*, 498, 579
- Gómez-Guijarro, C., Toft, S., Karim, A., et al. 2018, *ApJ*, 856, 121
- González-Alfonso, E., Fischer, J., Spoon, H. W. W., et al. 2017, *ApJ*, 836, 11
- González-Alfonso, E., Fischer, J., Sturm, E., et al. 2015, *ApJ*, 800, 69
- González-Alfonso, E., Pereira-Santaella, M., Fischer, J., et al. 2021, *A&A*, 645, A49
- González-Alfonso, E. & Sakamoto, K. 2019, *ApJ*, 882, 153
- Gullberg, B., Swinbank, A. M., Smail, I., et al. 2018, *ApJ*, 859, 12
- Hardcastle, M. J. & Croston, J. H. 2020, *New A Rev.*, 88, 101539
- Hayashi, T. J., Hagiwara, Y., & Imanishi, M. 2021, *arXiv e-prints*, arXiv:2101.12058
- Helfand, D. J., White, R. L., & Becker, R. H. 2015, *ApJ*, 801, 26
- Hernán-Caballero, A., Spoon, H. W. W., Alonso-Herrero, A., et al. 2020, *MNRAS*, 497, 4614
- Hopkins, P. F., Cox, T. J., Hernquist, L., et al. 2013, *MNRAS*, 430, 1901
- Houck, J. R., Roellig, T. L., van Cleve, J., et al. 2004, *ApJS*, 154, 18
- Imanishi, M., Imase, K., Oi, N., & Ichikawa, K. 2011, *AJ*, 141, 156
- Imanishi, M., Kawamuro, T., Kikuta, S., Nakano, S., & Saito, Y. 2020, *ApJ*, 891, 140
- Imanishi, M., Nakanishi, K., & Izumi, T. 2016, *AJ*, 152, 218
- Imanishi, M., Nakanishi, K., & Izumi, T. 2019, *ApJS*, 241, 19
- Imanishi, M. & Terashima, Y. 2004, *AJ*, 127, 758
- Iwasawa, K., Sanders, D. B., Teng, S. H., et al. 2011, *A&A*, 529, A106+
- Jiang, B. W., Gao, J., Omont, A., Schuller, F., & Simon, G. 2006, *A&A*, 446, 551
- Kennicutt, R. C. & Evans, N. J. 2012, *ARA&A*, 50, 531
- Kim, D., Veilleux, S., & Sanders, D. B. 1998, *ApJ*, 508, 627
- Klaas, U., Haas, M., Müller, S. A. H., et al. 2001, *A&A*, 379, 823
- Kovács, A., Omont, A., Beelen, A., et al. 2010, *ApJ*, 717, 29
- Kroupa, P. 2001, *MNRAS*, 322, 231
- Lahuis, F., Spoon, H. W. W., Tielens, A. G. G. M., et al. 2007, *ApJ*, 659, 296
- Lebouteiller, V., Barry, D. J., Spoon, H. W. W., et al. 2011, *ApJS*, 196, 8
- Leipski, C., Falcke, H., Bennert, N., & Hüttemeister, S. 2006, *A&A*, 455, 161
- Leitherer, C., Schaerer, D., Goldader, J. D., et al. 1999, *ApJS*, 123, 3
- Leroy, A. K., Evans, A. S., Momjian, E., et al. 2011, *ApJ*, 739, L25
- Lonsdale, C. J., Farrah, D., & Smith, H. E. 2006, *Ultraluminous Infrared Galaxies*, ed. Mason, J. W. (Springer Verlag), 285+
- Lutz, D., Sturm, E., Janssen, A., et al. 2020, *A&A*, 633, A134
- Marconi, A., Risaliti, G., Gilli, R., et al. 2004, *MNRAS*, 351, 169
- Mauch, T., Murphy, T., Buttery, H. J., et al. 2003, *MNRAS*, 342, 1117
- McMullin, J. P., Waters, B., Schiebel, D., Young, W., & Golap, K. 2007, in *Astronomical Society of the Pacific Conference Series*, Vol. 376, *Astronomical Data Analysis Software and Systems XVI*, ed. R. A. Shaw, F. Hill, & D. J. Bell, 127
- Meyers, B. W., Hurley-Walker, N., Hancock, P. J., et al. 2017, *PASA*, 34, e013
- Michiyama, T., Iono, D., Nakanishi, K., et al. 2020, *ApJ*, 895, 85
- Moshir, M. & et al. 1990, *IRAS Faint Source Catalogue*, 0
- Murphy, E. J., Condon, J. J., Schinnerer, E., et al. 2011, *ApJ*, 737, 67
- Murphy, T., Mauch, T., Green, A., et al. 2007, *MNRAS*, 382, 382
- Nagar, N. M., Wilson, A. S., Falcke, H., Veilleux, S., & Maiolino, R. 2003, *A&A*, 409, 115
- Nardini, E., Risaliti, G., Salvati, M., et al. 2008, *MNRAS*, 385, L130
- Nardini, E., Risaliti, G., Salvati, M., et al. 2009, *MNRAS*, 399, 1373
- Nardini, E., Risaliti, G., Watabe, Y., Salvati, M., & Sani, E. 2010, *MNRAS*, 405, 2505
- Oh, K., Koss, M., Markwardt, C. B., et al. 2018, *ApJS*, 235, 4
- Oteo, I., Zwaan, M. A., Ivison, R. J., Smail, I., & Biggs, A. D. 2017, *ApJ*, 837, 182
- Padoan, P., Haugbølle, T., & Nordlund, Å. 2012, *ApJ*, 759, L27
- Pearson, C., Rigopoulou, D., Hurley, P., et al. 2016, *ApJS*, 227, 9
- Pereira-Santaella, M., Colina, L., García-Burillo, S., et al. 2018, *A&A*, 616, A171
- Pereira-Santaella, M., Colina, L., García-Burillo, S., et al. 2016, *A&A*, 587, A44
- Pereira-Santaella, M., González-Alfonso, E., Usero, A., et al. 2017, *A&A*, 601, L3
- Perna, M., Arribas, S., Catalán-Torrecilla, C., et al. 2020, *A&A*, 643, A139
- Perna, M., Arribas, S., Pereira Santaella, M., et al. 2021, *A&A*, 646, A101
- Petric, A. O., Ho, L. C., Flagey, N. J. M., & Scoville, N. Z. 2015, *ApJS*, 219, 22
- Planck Collaboration, Abergel, A., Ade, P. A. R., et al. 2011, *A&A*, 536, A25
- Ricci, C., Bauer, F. E., Treister, E., et al. 2017, *MNRAS*, 468, 1273
- Riechers, D. A., Leung, T. K. D., Ivison, R. J., et al. 2017, *ApJ*, 850, 1
- Rieke, G. H., Young, E. T., Engelbracht, C. W., et al. 2004, *ApJS*, 154, 25
- Sakamoto, K., Aalto, S., Barcos-Muñoz, L., et al. 2017, *ApJ*, 849, 14
- Sakamoto, K., Aalto, S., Costagliola, F., et al. 2013, *ApJ*, 764, 42
- Sanders, D. B., Mazzarella, J. M., Kim, D.-C., Surace, J. A., & Soifer, B. T. 2003, *AJ*, 126, 1607
- Sanders, D. B., Soifer, B. T., Elias, J. H., et al. 1988, *ApJ*, 325, 74
- Scoville, N., Murchikova, L., Walter, F., et al. 2017, *ApJ*, 836, 66
- Sliwa, K., Wilson, C. D., Aalto, S., & Privon, G. C. 2017, *ApJ*, 840, L11
- Soifer, B. T., Neugebauer, G., Matthews, K., et al. 2000, *AJ*, 119, 509
- Spoon, H. W. W., Farrah, D., Lebouteiller, V., et al. 2013, *ApJ*, 775, 127
- Spoon, H. W. W., Marshall, J. A., Houck, J. R., et al. 2007, *ApJ*, 654, L49
- Springel, V., Di Matteo, T., & Hernquist, L. 2005, *MNRAS*, 361, 776
- Stanghellini, C., O'Dea, C. P., Dallacasa, D., et al. 1998, *A&AS*, 131, 303
- Sturm, E., González-Alfonso, E., Veilleux, S., et al. 2011, *ApJ*, 733, L16
- Teng, S. H., Rigby, J. R., Stern, D., et al. 2015, *ApJ*, 814, 56
- Thompson, T. A., Quataert, E., & Murray, N. 2005, *ApJ*, 630, 167
- Ueda, J., Iono, D., Yun, M. S., et al. 2014, *ApJS*, 214, 1
- Veilleux, S., Rupke, D. S. N., Kim, D.-C., et al. 2009, *ApJS*, 182, 628
- Weigel, A. K., Schawinski, K., Caplar, N., et al. 2017, *ApJ*, 845, 145
- Weinberger, R., Springel, V., Pakmor, R., et al. 2018, *MNRAS*, 479, 4056
- Wilson, C. D., Rangwala, N., Glenn, J., et al. 2014, *ApJ*, 789, L36
- Wright, A. E., Griffith, M. R., Burke, B. F., & Ekers, R. D. 1994, *ApJS*, 91, 111
- Xu, C. K., Cao, C., Lu, N., et al. 2015, *ApJ*, 799, 11

Appendix A: Mid-IR *Spitzer* observations of the ULIRGs

Table A.1: *Spitzer* IRS and MIPS fluxes and $9.7\mu\text{m}$ silicate strength

IRAS name	$S_{9.7\mu\text{m}}^a$	IRS $34\mu\text{m}^b$	MIPS $70\mu\text{m}$	MIPS $160\mu\text{m}$
00091–0738	-3.20 ± 0.12	1.07
00188–0856	-2.72 ± 0.08	0.80	2.65	1.91
00509+1225	0.30 ± 0.01	1.34
01572+0009	0.19 ± 0.02	1.17
F05189–2524	-0.32 ± 0.01	7.30
07251–0248	-2.77 ± 0.06	2.62
09022–3615	-1.04 ± 0.01	3.53
F10190+1322	-1.09 ± 0.02	0.85	3.55	...
11095–0238	-3.43 ± 0.07	1.54	2.95	1.28
F12072–0444	-1.42 ± 0.02	1.20
F12112+0305	-1.35 ± 0.03	2.06
13120–5453	-1.18 ± 0.01	10.1
F13451+1232	-0.32 ± 0.02	1.03	2.04	1.41
F14348–1447	-1.89 ± 0.03	1.98
F14378–3651	-1.44 ± 0.05	1.85
F15327+2340	-2.74 ± 0.01	34.4
16090–0139	-2.65 ± 0.06	1.07
16155+0146	-2.41 ± 0.07	0.75
17208–0014	-1.56 ± 0.01	8.67
F19297–0406	-1.49 ± 0.04	2.12
19542+1110	-0.97 ± 0.02	2.19
20087–0308	-1.82 ± 0.04	0.99
20100–4156	-2.79 ± 0.06	1.81	4.56	2.33
20414–1651	-1.62 ± 0.08	1.25
F22491–1808	-1.19 ± 0.03	2.20

Notes. Fluxes are in Jy. The flux uncertainties are dominated by the $\sim 10\%$ calibration uncertainty. ^(a) $9.7\mu\text{m}$ silicate strength from the IDEOS database (Hernán-Caballero et al. 2020, Spoon et al. in prep.) based on the IRS spectroscopy of these ULIRGs. ^(b) $34\mu\text{m}$ observed wavelength flux measured in the *Spitzer*/IRS spectrum.

Appendix B: ALMA continuum models

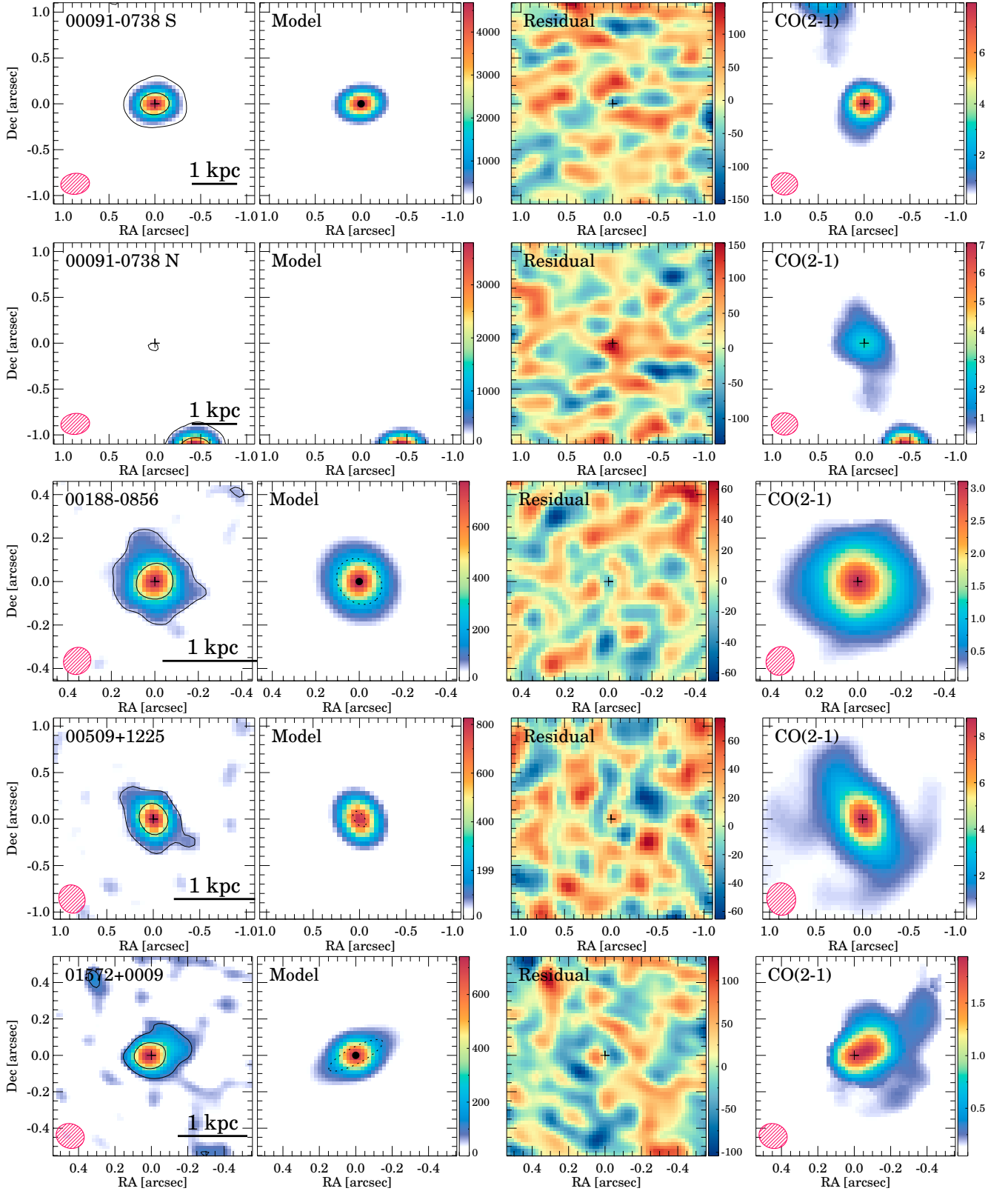


Fig. B.1: Same as Fig. 1.

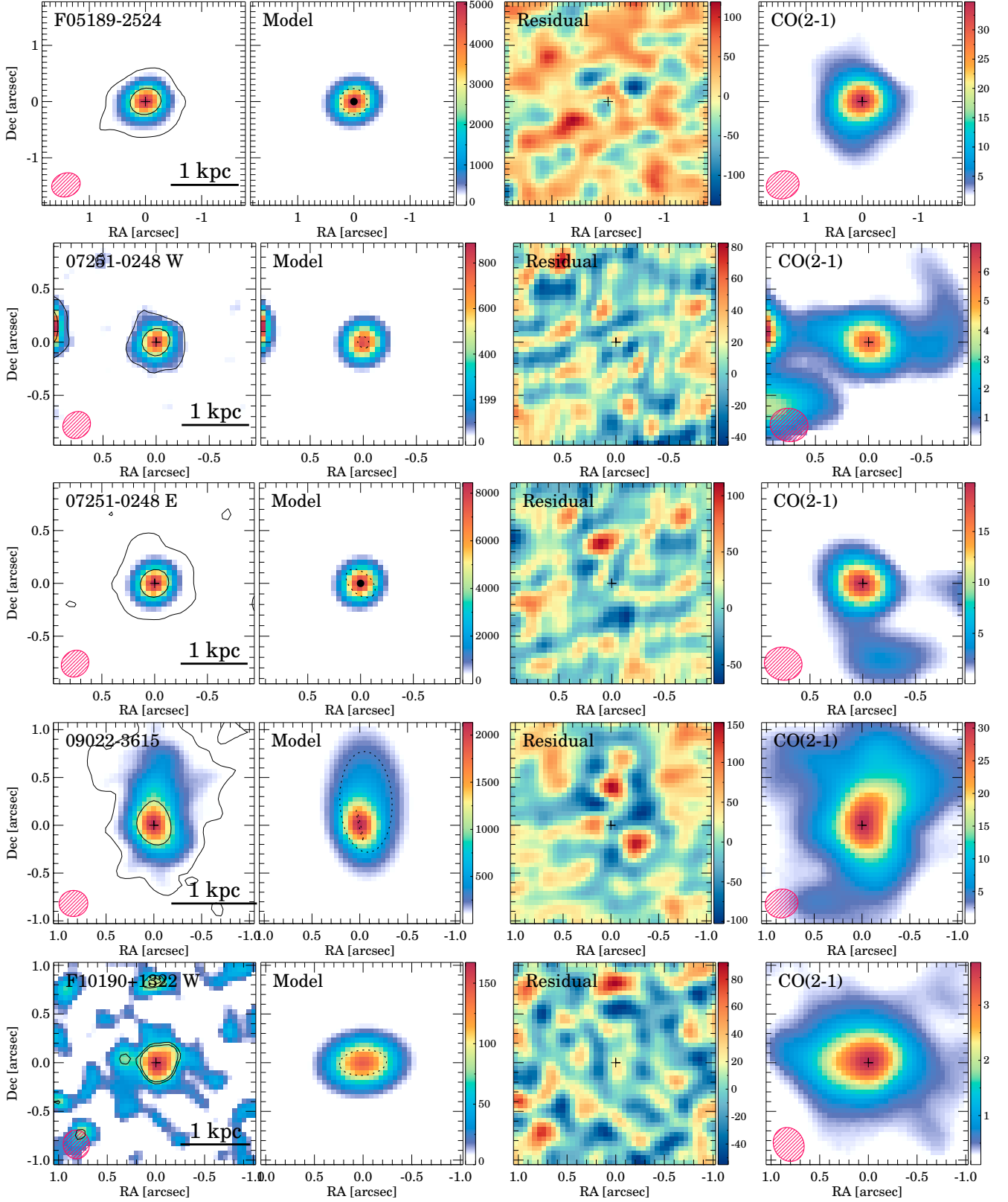


Fig. B.1: (Continued)

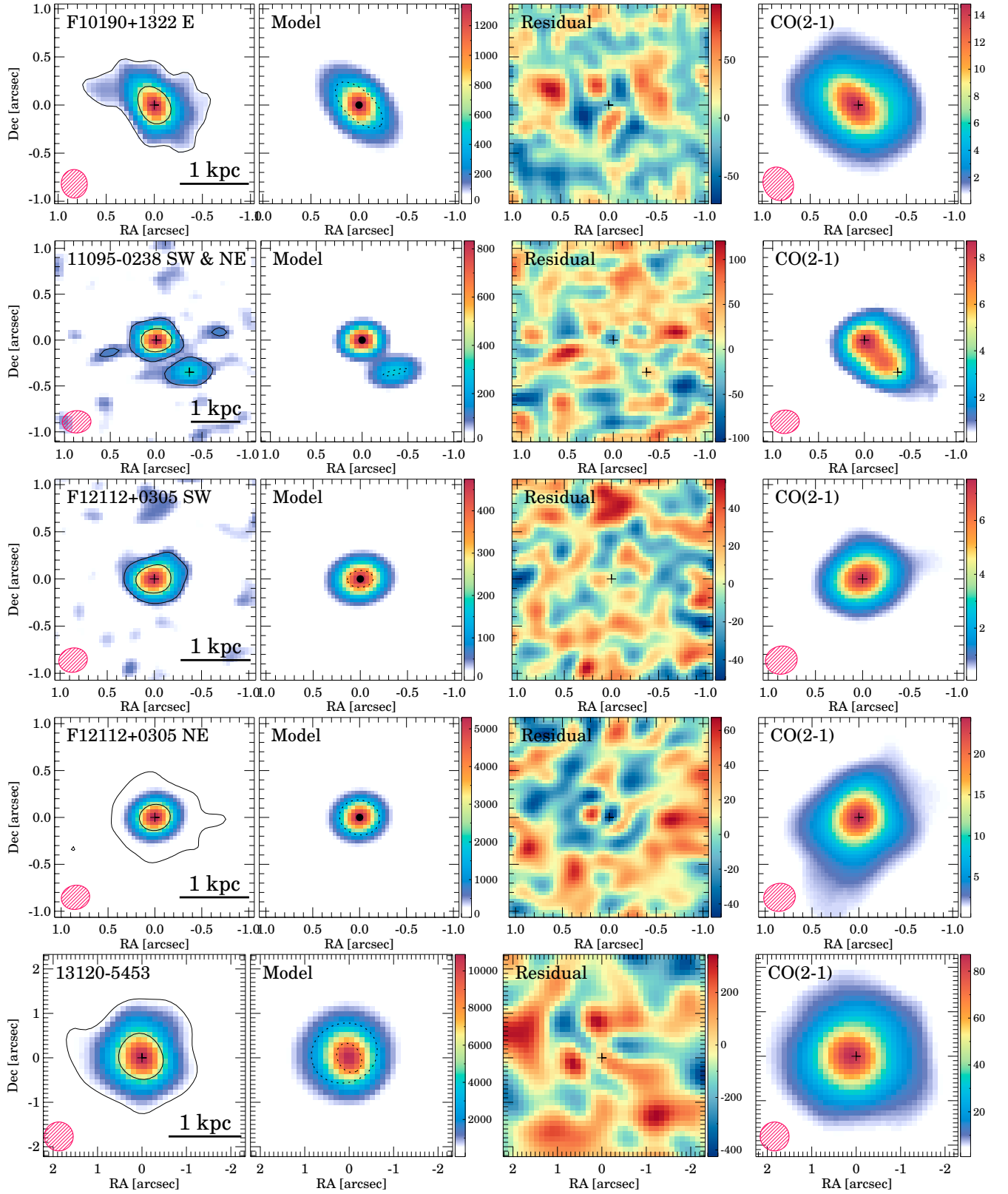


Fig. B.1: (Continued)

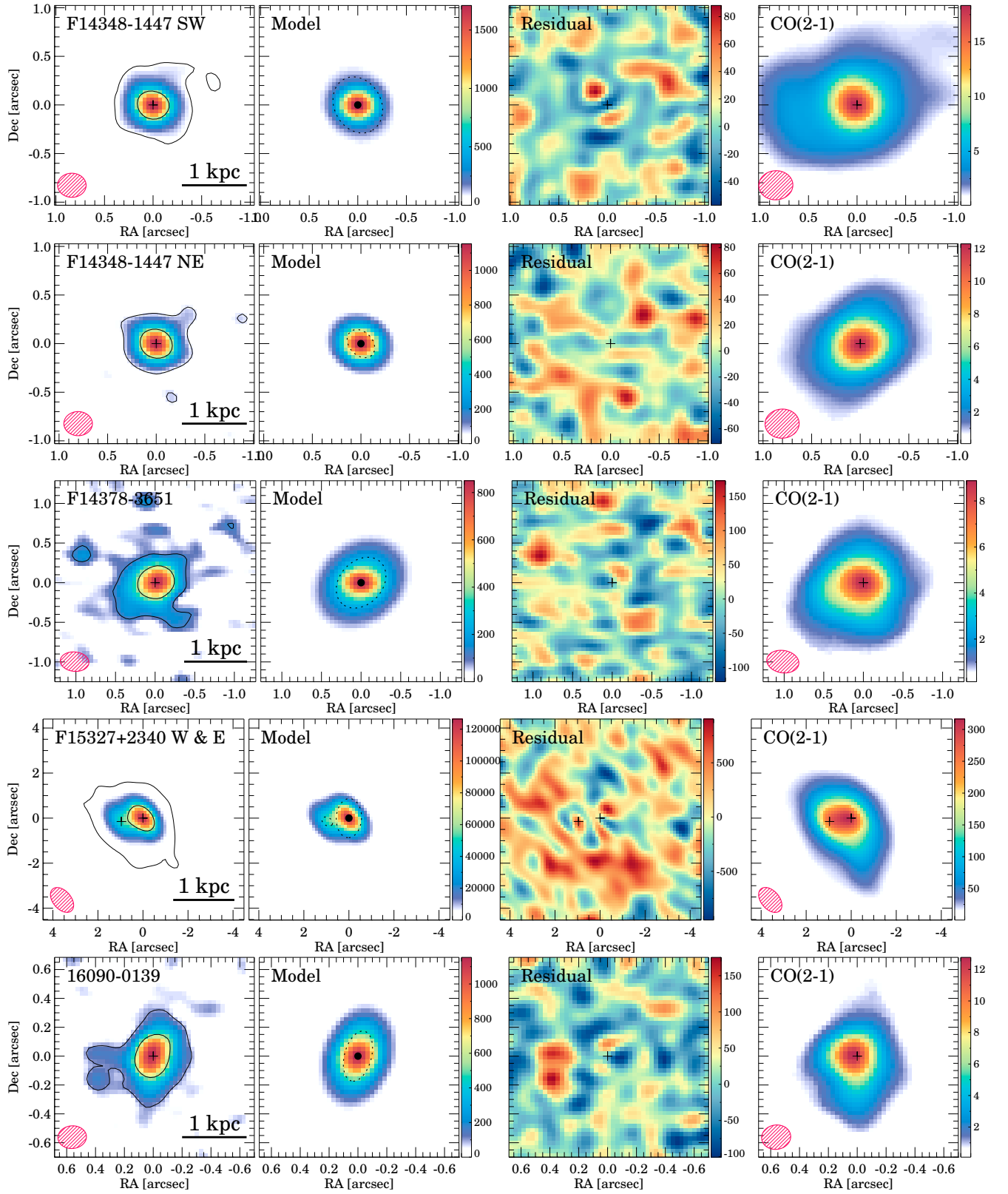


Fig. B.1: (Continued)

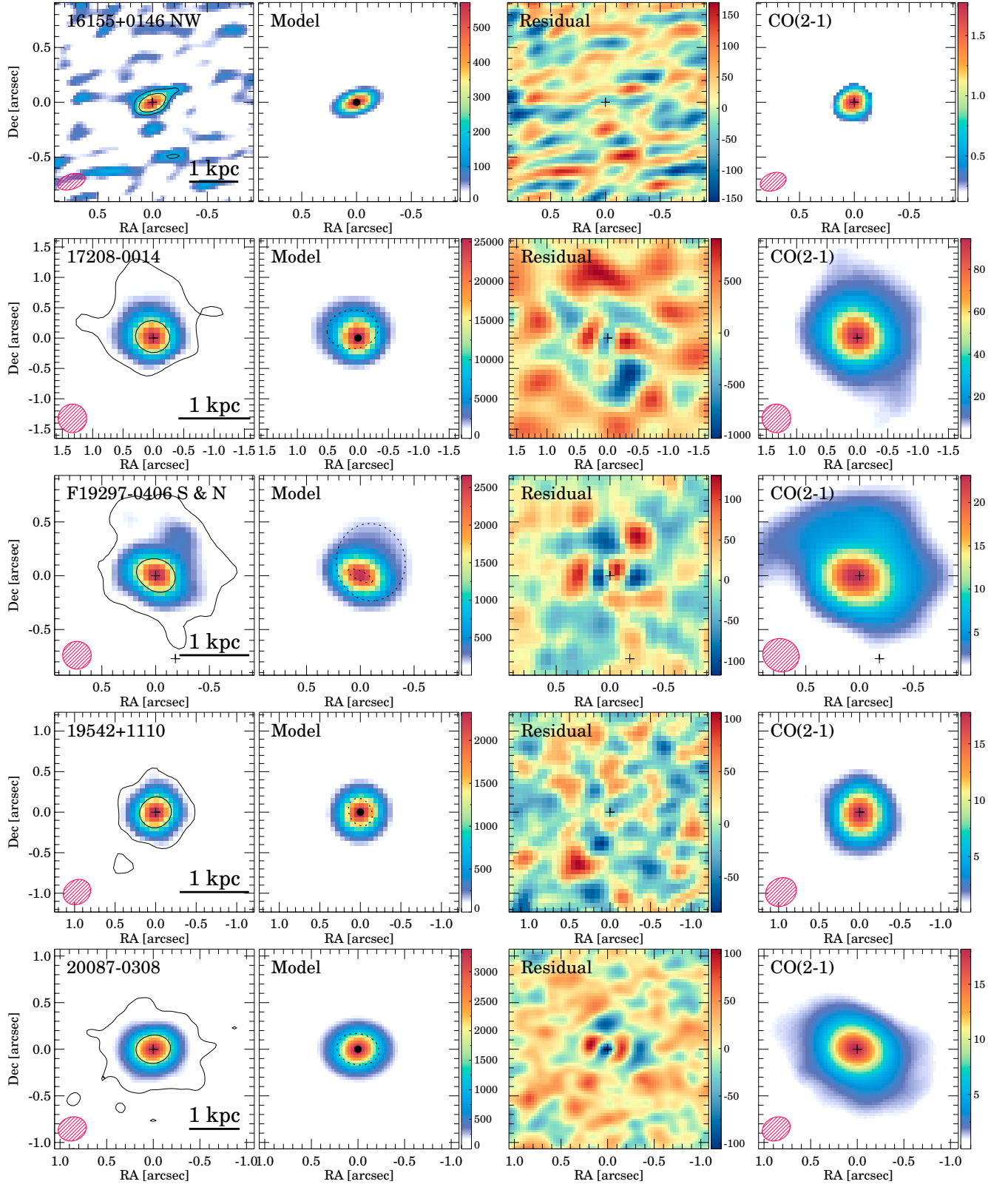


Fig. B.1: (Continued)

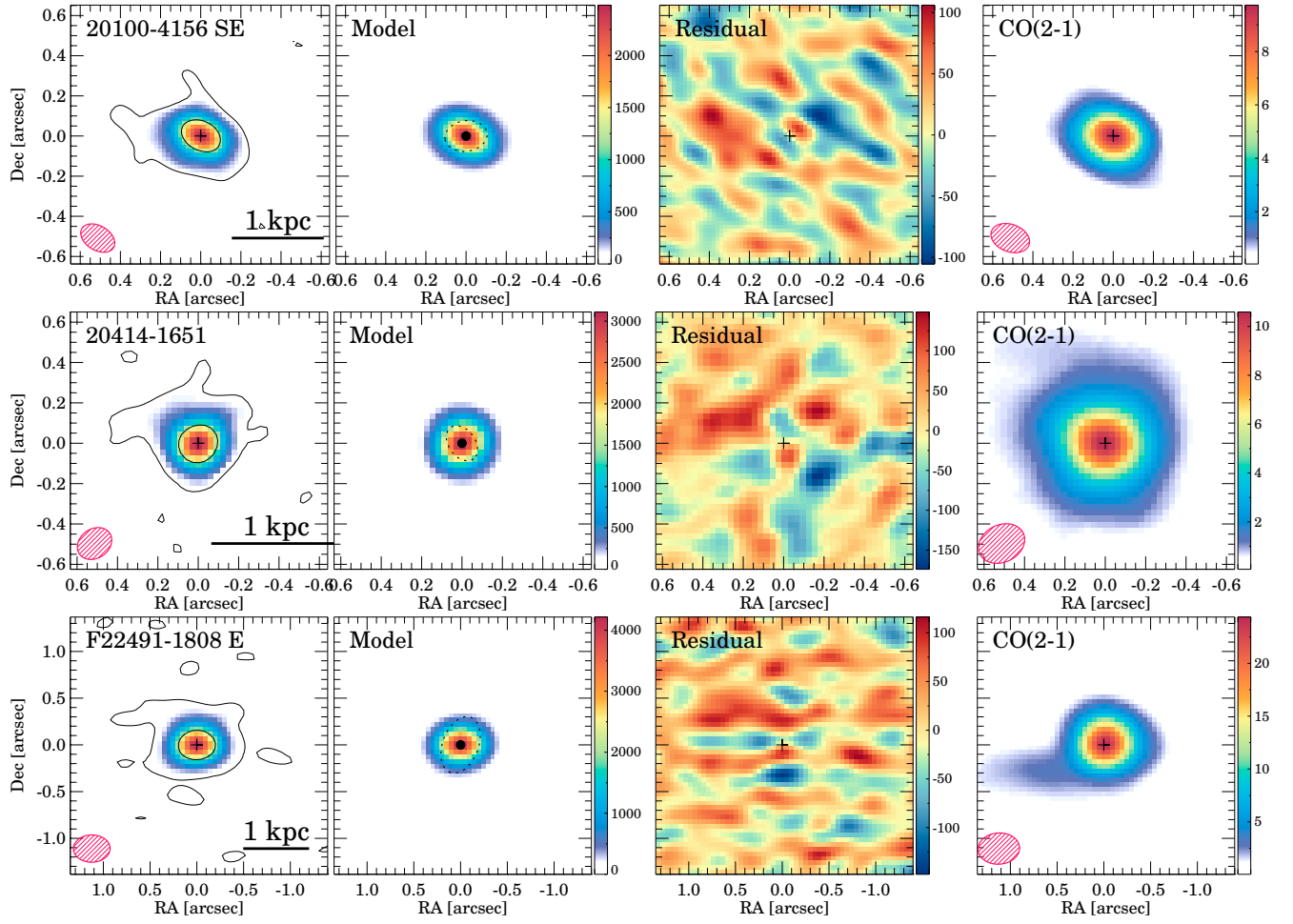


Fig. B.1: (Continued)

Appendix C: CO(2–1) emission models

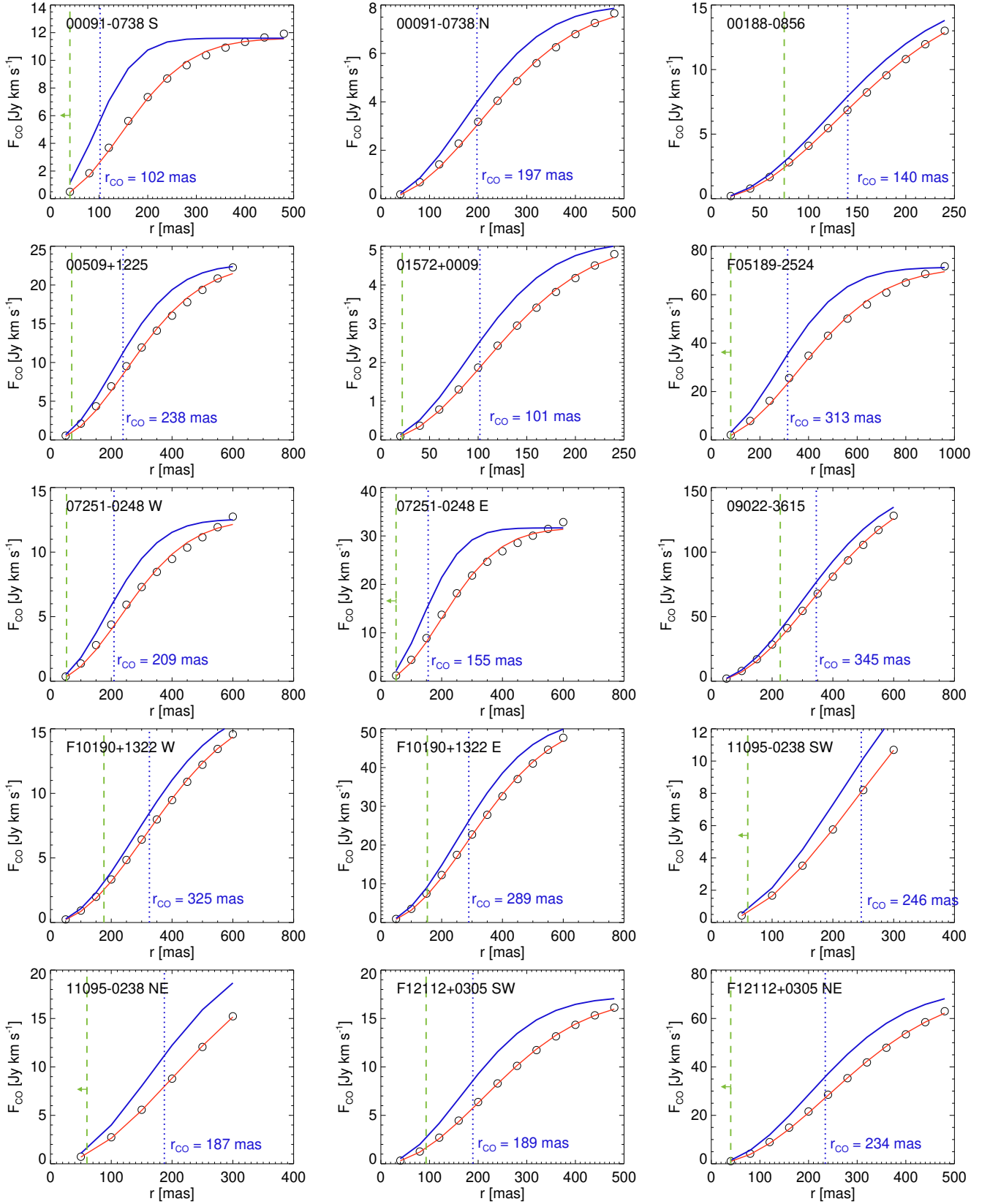


Fig. C.1: Same as Fig. 4.

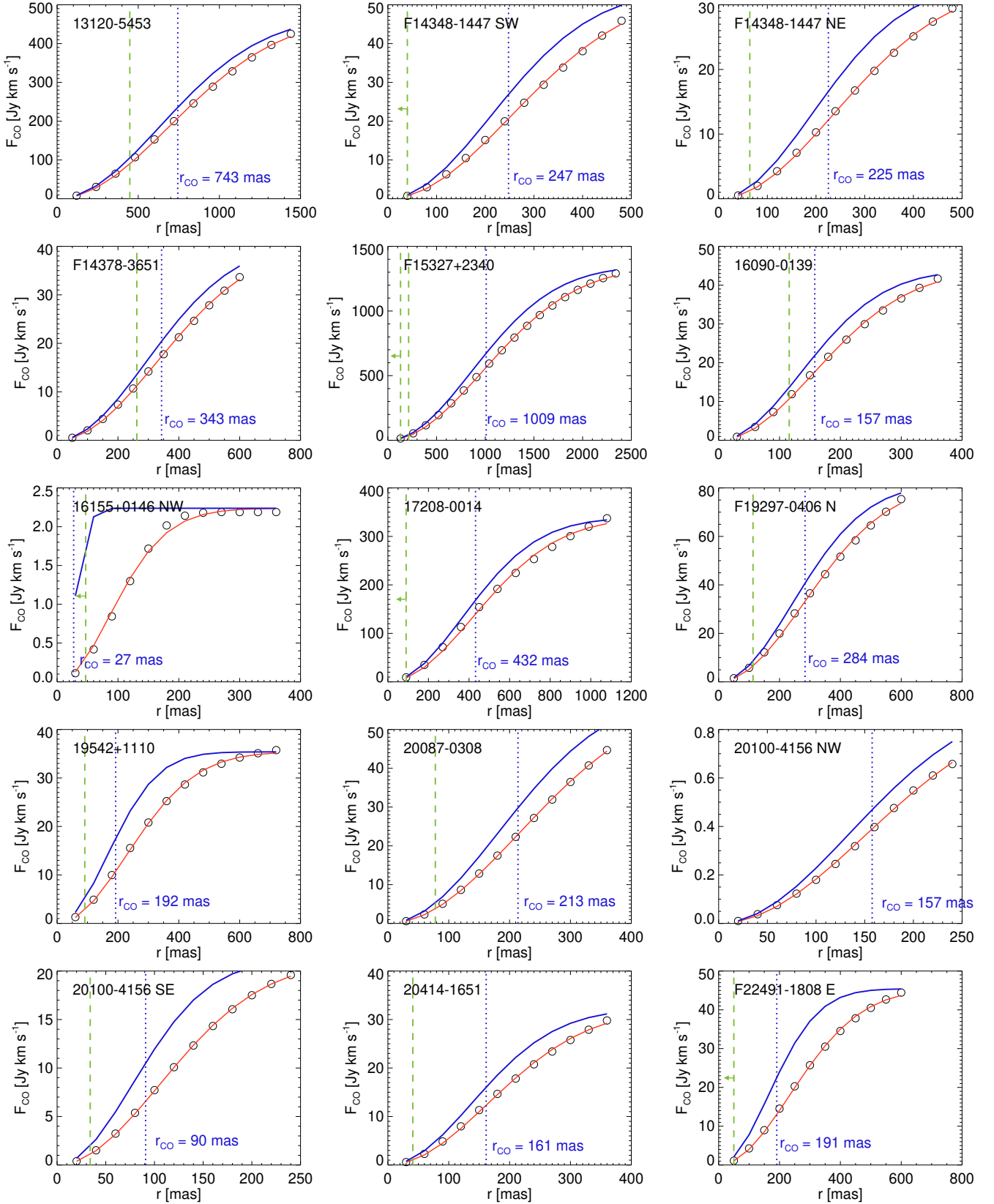


Fig. C.1: (Continued)

Appendix D: SED models

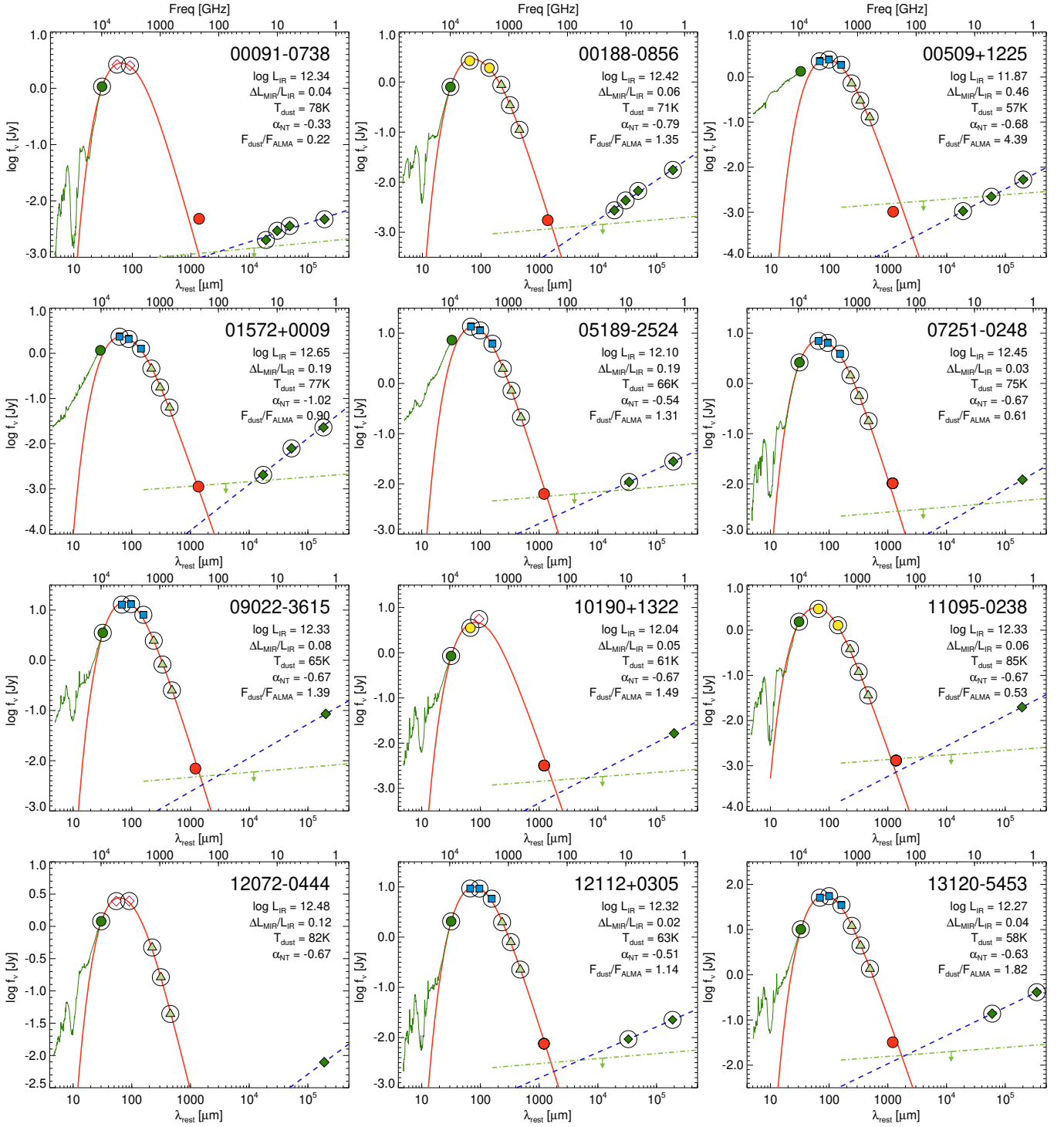


Fig. D.1: Same as Fig. 6. The IR observations are color coded as follows: *Spitzer*/IRS synthetic photometry at $34\mu\text{m}$ (green circle); *Spitzer*/MIPS (yellow circles); *IRAS* (purple diamonds); *Herschel*/PACS (blue squares); *ISO*/ISOPHOT (blue circles); and *Herschel*/SPIRE (green triangles).

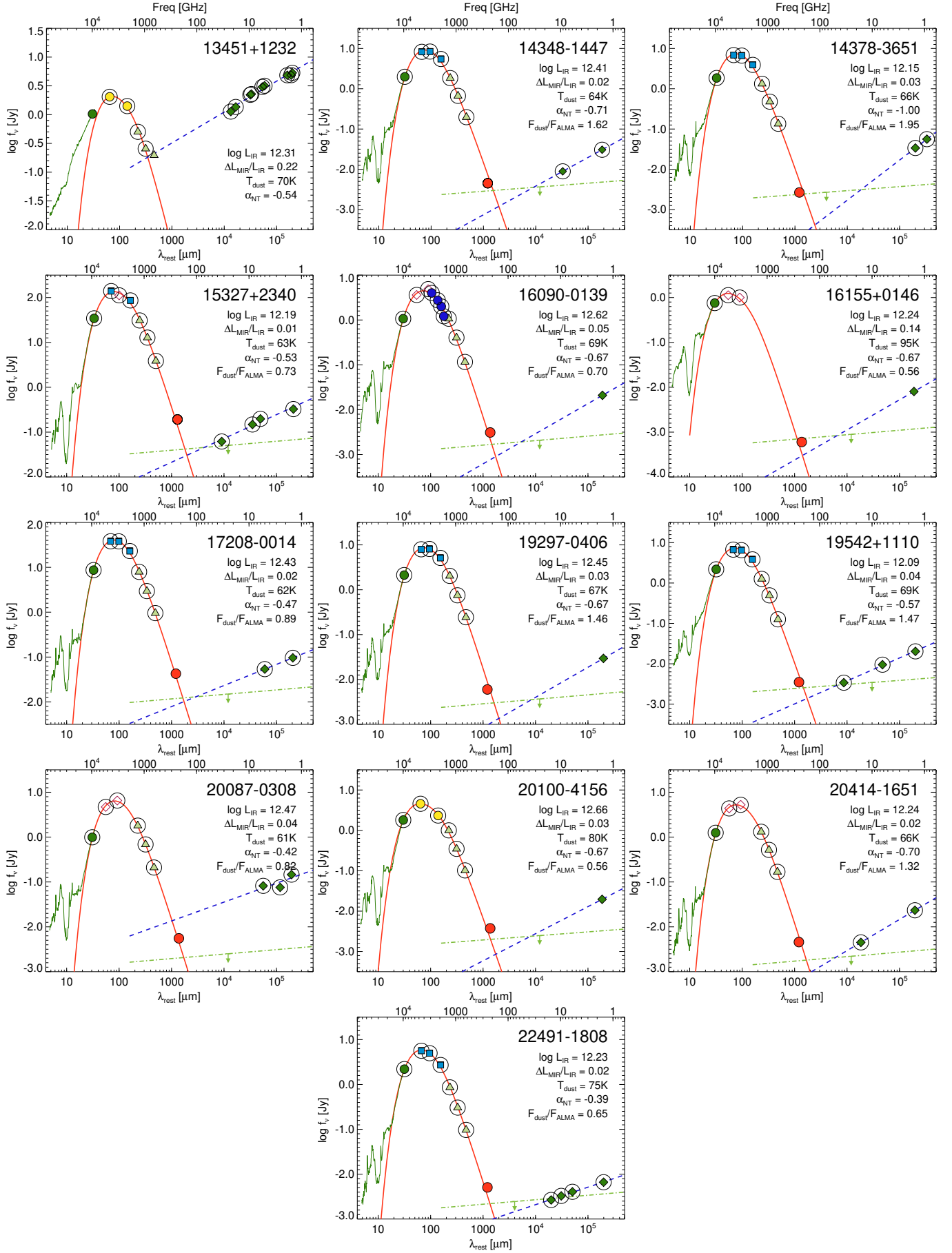


Fig. D.1: (Continued)